Commun. Comput. Phys.
doi: 10.4208/cicp.301110.040811a

Vol. **12**, No. 3, pp. 613-661
September 2012

REVIEW ARTICLE

Phase-Field Models for Multi-Component Fluid Flows

Junseok Kim*

Department of Mathematics, Korea University, Seoul 136-701, Republic of Korea.

Received 30 November 2010; Accepted (in revised version) 4 August 2011

Communicated by Rho Shin Myong

Available online 1 March 2012

Abstract. In this paper, we review the recent development of phase-field models and their numerical methods for multi-component fluid flows with interfacial phenomena. The models consist of a Navier-Stokes system coupled with a multi-component Cahn-Hilliard system through a phase-field dependent surface tension force, variable density and viscosity, and the advection term. The classical infinitely thin boundary of separation between two immiscible fluids is replaced by a transition region of a small but finite width, across which the composition of the mixture changes continuously. A constant level set of the phase-field is used to capture the interface between two immiscible fluids. Phase-field methods are capable of computing topological changes such as splitting and merging, and thus have been applied successfully to multi-component fluid flows involving large interface deformations. Practical applications are provided to illustrate the usefulness of using a phase-field method. Computational results of various experiments show the accuracy and effectiveness of phase-field models.

AMS subject classifications: 76D05, 76D45, 76T30, 82C26

Key words: Navier-Stokes, Cahn-Hilliard, multi-component, surface tension, interface dynamics, interface capturing, phase-field model.

Contents

*Corresponding author. *Email address:* cfdkim@korea.ac.kr (J. S. Kim)

1 Introduction

Many important industrial problems involve flows with multiple constitutive components. Several examples are the impact of a droplet on a solid surface [53], bubbly and slug flows in a microtube [46], drop coalescence and retraction in viscoelastic fluids [106], and realistic interfaces in computer graphics [1]. Due to inherent nonlinearities, topological changes, and the complexity of dealing with unknown moving interfaces, multiphase flows are challenging to study from mathematical modeling and numerical algorithmic points of view.

There are many ways to characterize moving interfaces. The two main approaches to simulating multiphase and multi-component flows are interface tracking and interface capturing methods. In interface tracking methods (volume-of-fluid [42], front-tracking [40], and immersed boundary [49,50,80,81,96]), Lagrangian particles are used to track the interfaces and are advected by the velocity field. In interface capturing methods such as level-set [24,78,79,85,91,92] and phase-field methods [4,6,13,29,46,47,54,56,74,86,90,102], the interface is implicitly captured by a contour of a particular scalar function.

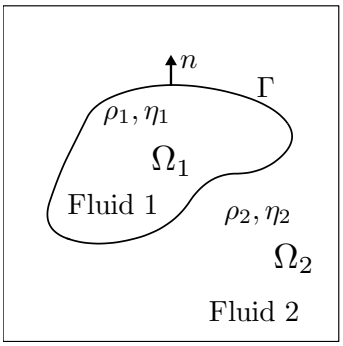

Figure 1: Schematic diagram of a two phase domain.

The governing equations of unsteady, viscous, incompressible, and immiscible two fluid systems in three-dimensional space are the Navier-Stokes equations:

$$\rho_i\left(\frac{\partial \mathbf{u}_i}{\partial t}+\mathbf{u}_i\cdot\nabla\mathbf{u}_i\right)=-\nabla p_i+\nabla\cdot[\eta_i(\nabla\mathbf{u}_i+\nabla\mathbf{u}_i^T)]+\rho_i\mathbf{g}, \qquad \text{in } \Omega_i,$$
$$\nabla\cdot\mathbf{u}_i=0, \qquad \text{in } \Omega_i,$$

where $\rho_i(\mathbf{x},t)$ is the density, $\mathbf{u}_i(\mathbf{x},t)=(u_1(\mathbf{x},t),u_2(\mathbf{x},t),u_3(\mathbf{x},t))$ is the velocity, $p_i(\mathbf{x},t)$ is the pressure, and $\eta_i(\mathbf{x},t)$ is the viscosity of fluid $i=1,2$, the superscript T denotes transpose, and $\mathbf{g}$ is the gravitational force per unit mass. See Fig. 1 for the schematic diagram of a two phase domain. Γ is the interface of the two immiscible fluids and $\mathbf{n}=(n_1,n_2,n_3)$ is the unit normal vector to the interface. On the interface Γ, we have a normal jump condition

$$p_2-p_1=\sigma\kappa+\left(2\eta n_k\frac{\partial u_k}{\partial n}\right)_2-\left(2\eta n_k\frac{\partial u_k}{\partial n}\right)_1,$$

https://doi.org/10.4208/cicp.301110.040811a Published online by Cambridge University Press

where σ is the surface tension coefficient and κ is the mean curvature of the interface [97]. The above equation implies that both the surface tension and the viscous stress at the interface contribute to the pressure jump. For immiscible and incompressible multi-component fluid flows, the governing equations can be written as

$$\rho(\mathbf{u}_t+\mathbf{u}\cdot\nabla\mathbf{u})=-\nabla p+\nabla\cdot[\eta(\nabla\mathbf{u}+\nabla\mathbf{u}^T)]+\mathbf{SF}_{sing}+\rho\mathbf{g}, \tag{1.1a}$$

$$\nabla\cdot\mathbf{u}=0, \qquad \text{in } \Omega=\Omega_1\cup\Omega_2, \tag{1.1b}$$

where $\mathbf{SF}_{sing}=-\sigma\kappa\delta_\Gamma\mathbf{n}$ is the singular surface tension force (δ_Γ is the surface delta function) [56].

In this paper, we focus on the review of mathematical models and numerical methods for multi-component fluids using phase-field methods. The contents of this paper are organized as follows. In Section 2, phase-field models for multi-component fluid flows are presented. In Section 3, numerical solutions for phase-field models are described. In Section 4, numerical applications are described. Numerical experiments are presented in Section 5. In Section 6, conclusions are given.

2 Phase-field models

Phase field models are an increasingly popular choice for modeling the motion of multiphase fluids. The basic idea is to introduce a conserved order parameter such as a mass concentration that varies continuously over thin interfacial layers and is mostly uniform in the bulk phases. In the phase-field model, sharp fluid interfaces are replaced by thin but nonzero thickness transition regions where the interfacial forces are smoothly distributed. In D. M. Anderson, G. B. McFadden, and A. A. Wheeler's review paper (1998) [4], the authors reviewed the development of diffuse-interface models of hydrodynamics and their application to a wide variety of interfacial phenomena. However, since then many new models, numerical solutions, and applications have emerged and we want to address these improvements in this paper. Examples are modeling ternary fluids [14,59,64], the adaptive mesh method [15], drop coalescence and retraction in viscoelastic fluids [106], and contact angle boundary conditions [29,45,48,55,67,104].

2.1 A binary fluid

We now consider the incompressible flow of two immiscible fluids. The phase-field is defined to be either the difference between [73] or the fraction of one of [56] the concentrations of the two mixtures

$$\phi=\frac{m_1-m_2}{m_1+m_2}, \qquad c=\frac{m_1}{m_1+m_2}, \tag{2.1}$$

where m_1 and m_2 are the masses of fluids 1 and 2. We note that $-1\le\phi\le1$ and $0\le c\le1$. Throughout this paper, we will use ϕ and c as phase-fields defined by Eq. (2.1). The

https://doi.org/10.4208/cicp.301110.040811a Published online by Cambridge University Press

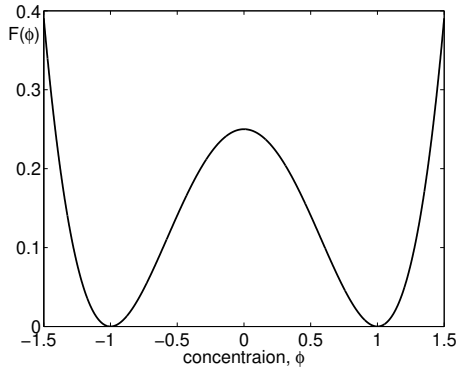

Figure 2: Double well potential. $F(\phi)=0.25(\phi^2-1)^2$.

phase-field is also called by an order parameter [25]. The governing equation for the phase-field is the advective Cahn-Hilliard (CH) equation:

$$\phi_t+\mathbf{u}\cdot\nabla\phi=\nabla\cdot(M(\phi)\nabla\mu), \tag{2.2a}$$

$$\mu=F'(\phi)-\epsilon^2\Delta\phi, \tag{2.2b}$$

where $\mathbf{u}$ is the bulk velocity and $M(\phi)$ is the phase-field dependent non-negative mobility; $M(c)=c(1-c)$ is used in [56], $M(\phi)=1-\phi^2$ is used in [6], and $M(c)=1$ is used in [12]. In the variable mobility case, the Cahn-Hilliard dynamics is controlled by interface diffusion and in the constant mobility case, it is controlled by bulk diffusion. $F(\phi)=0.25(\phi^2-1)^2$ is the Helmholtz free energy of a unit volume of homogeneous material of composition ϕ (see Fig. 2). ϵ is a positive constant, which is related to the thickness of the interfacial transition of the phase-field. We also have $F(c)=0.25c^2(c-1)^2$ for the concentration variable c.

The CH equation without flow arises from the Ginzburg-Landau free energy

$$\mathcal{E}(\phi):=\int_\Omega\left(F(\phi)+\frac{\epsilon^2}{2}|\nabla\phi|^2\right)d\mathbf{x},$$

where Ω is the region of space occupied by the system [19, 20]. To obtain the CH equation with a variable mobility, one introduces a chemical potential μ as the variational derivative of $\mathcal{E}$, $\mu:=\delta\mathcal{E}/\delta\phi=F'(\phi)-\epsilon^2\Delta\phi$ and defines the flux as $\mathcal{J}:=-M(\phi)\nabla\mu$. As a consequence of mass conservation, we have $\partial\phi/\partial t=-\nabla\cdot\mathcal{J}$, which is the CH equation with a variable mobility. Please refer to [19, 20, 77, 109] for more details about the basic physical principle of CH equation. The natural and no-flux boundary conditions are

$$\frac{\partial\phi}{\partial n}=\nabla\phi\cdot\mathbf{n}=0 \text{ and } \mathcal{J}\cdot\mathbf{n}=0 \text{ on } \partial\Omega, \quad \text{where } \mathbf{n} \text{ is a unit normal vector to } \partial\Omega. \tag{2.3}$$

Next, we review a mathematical derivation of the Cahn-Hilliard equation as a gradient

https://doi.org/10.4208/cicp.301110.040811a Published online by Cambridge University Press

flow [35]:

$$\frac{\partial\phi}{\partial t}=-M\text{grad}_0\mathcal{E}(\phi), \tag{2.4}$$

where M is a positive constant and the symbol "grad_0" here denotes a constrained gradient in a Hilbert space, defined by $\int_\Omega\phi d\mathbf{x}=$ constant. Let the domain $\mathcal{D}$ of the functional $\mathcal{E}$ be the set of smooth enough functions ϕ defined in Ω and satisfying $\partial\phi/\partial\mathbf{n}=0$. Considering $\phi-\frac{1}{|\Omega|}\int_\Omega\phi d\mathbf{x}$, we may consider functions with zero average. Let $\dot{H}^1$ be the zero-average subspace of the Hilbert $H^1=W^{1,2}(\Omega)$, with norm $\|\nabla u\|_{L^2}$ and inner product $(u,v)_{\dot{H}^1}\equiv(\nabla u,\nabla v)_{L^2}$ for $u,v\in\dot{H}^1$. Denote by $\dot{H}^{-1}$ the zero-average subspace of the dual $(H^1)^*$ of the Hilbert space H^1. The inner product of $u,v\in\dot{H}^{-1}$ is defined by

$$(u,v)_{\dot{H}^{-1}}\equiv(\nabla\phi_u,\nabla\phi_v)_{L^2},$$

where $\phi_u,\phi_v\in\dot{H}^1$ are the associates of u,v. For example [39], ϕ_u satisfies

$$\Delta\phi_u=u \text{ in } \Omega, \qquad \frac{\partial\phi_u}{\partial\mathbf{n}}=0 \text{ on } \partial\Omega, \qquad \int_\Omega\phi_u d\mathbf{x}=0.$$

Then, grad_0 is defined in the following way: Let $\dot{C}_0^\infty(\Omega)$ be the set of smooth functions with compact support and with zero average. Then, $\dot{C}_0^\infty$ is dense in $\dot{H}^{-1}$. Let ϕ be sufficiently smooth and satisfy $\partial\phi/\partial\mathbf{n}=\partial\Delta\phi/\partial\mathbf{n}=0$ on $\partial\Omega$. Then, we have that for all $v\in\dot{C}_0^\infty$,

$$\begin{aligned}(\text{grad}_0\mathcal{E}(\phi),v)_{\dot{H}^{-1}}&=\frac{d}{d\theta}\mathcal{E}(\phi+\theta v)\big|_{\theta=0}\\&=\lim_{\theta\to0}\frac{1}{\theta}(\mathcal{E}(\phi+\theta v)-\mathcal{E}(\phi))=\int_\Omega\big(F'(\phi)-\epsilon^2\Delta\phi\big)v d\mathbf{x}.\end{aligned} \tag{2.5}$$

Put $\Delta\phi_v$ in place of v in Eq. (2.5). An integration by parts then yields

$$\begin{aligned}&\int_\Omega[F'(\phi)-\epsilon^2\Delta\phi]\Delta\phi_v d\mathbf{x}=-\int_\Omega\nabla[F'(\phi)-\epsilon^2\Delta\phi]\cdot\nabla\phi_v d\mathbf{x}\\&=(-\nabla[F'(\phi)-\epsilon^2\Delta\phi],\nabla\phi_v)_{L^2}=(-\nabla\cdot\nabla[F'(\phi)-\epsilon^2\Delta\phi],\nabla\cdot\nabla\phi_v)_{\dot{H}^{-1}}\\&=(-\Delta[F'(\phi)-\epsilon^2\Delta\phi],v)_{\dot{H}^{-1}},\end{aligned}$$

where we have used the fact that $\nabla\phi_v$ has zero normal component on $\partial\Omega$. We identify

$$\text{grad}_0\mathcal{E}(\phi)\equiv-\Delta(F'(\phi)-\epsilon^2\Delta\phi) \tag{2.6}$$

and the ansatz (2.4) now gives us the law of motion

$$\phi_t=M\Delta(F'(\phi)-\epsilon^2\Delta\phi). \tag{2.7}$$

https://doi.org/10.4208/cicp.301110.040811a Published online by Cambridge University Press

We differentiate the energy $\mathcal{E}$ and the total mass $\int_\Omega \phi\, d\mathbf{x}$ to get

$$\begin{aligned}\frac{d}{dt}\mathcal{E}(t) &= \int_\Omega (F'(\phi)\phi_t + \epsilon^2 \nabla\phi\cdot\nabla\phi_t)d\mathbf{x} = \int_\Omega \mu\phi_t d\mathbf{x} = \int_\Omega \mu\nabla\cdot(M(\phi)\nabla\mu)d\mathbf{x} \\ &= \int_{\partial\Omega} \mu M(\phi)\frac{\partial\mu}{\partial n}ds - \int_\Omega \nabla\mu\cdot(M(\phi)\nabla\mu)d\mathbf{x} = -\int_\Omega M(\phi)|\nabla\mu|^2 d\mathbf{x} \end{aligned} \tag{2.8}$$

and

$$\frac{d}{dt}\int_\Omega \phi d\mathbf{x} = \int_\Omega \phi_t d\mathbf{x} = \int_\Omega \nabla\cdot(M(\phi)\nabla\mu)d\mathbf{x} = \int_{\partial\Omega} M(\phi)\frac{\partial\mu}{\partial n}ds = 0, \tag{2.9}$$

where we used the no-flux boundary condition (2.3). Therefore, the total energy is non-increasing in time and the total mass is conserved.

In 1958, Cahn and Hilliard derived the formulation of the free energy which takes into account the local free energy per molecule of a homogeneous system, $F(c)$ and the interfacial energy that results from composition gradients, $0.5\epsilon^2|\nabla c|^2$ [20]. In 1959, Cahn discussed the thermodynamic basis behind the free energy formulation [18]. In 1959, Cahn and Hilliard studied phase separation in immiscible liquid mixtures using the formulated free energy [21]. In 1961, Cahn discussed the study of spinodal decomposition in solids including the elastic stress effects due to the lattice parameter differences between the two phases [19]. These papers form the theoretical basis for almost all the diffuse interface studies on microstructural evolution in the metallurgical and materials science literature. If we put all the equations, (1.1a), (1.1b), (2.2a), and (2.2b), together, then we have

$$\rho(\phi)(\mathbf{u}_t + \mathbf{u}\cdot\nabla\mathbf{u}) = -\nabla p + \nabla\cdot[\eta(\phi)(\nabla\mathbf{u} + \nabla\mathbf{u}^T)] + \mathbf{SF} + \rho(\phi)\mathbf{g}, \tag{2.10a}$$

$$\nabla\cdot\mathbf{u} = 0, \tag{2.10b}$$

$$\phi_t + \mathbf{u}\cdot\nabla\phi = \nabla\cdot(M(\phi)\nabla\mu), \tag{2.10c}$$

$$\mu = F'(\phi) - \epsilon^2\Delta\phi. \tag{2.10d}$$

The singular force $\mathbf{SF}_{sing}$ is replaced by a regular force $\mathbf{SF}$ in terms of the phase-field, which will be defined later in Section 2.1.2.

In [107], authors examined the implications of Cahn-Hilliard diffusion on mass conservation when using a phase-field model for simulating two-phase flows. Even though the phase-field variable ϕ is conserved globally, a drop shrinks spontaneously while ϕ shifts from its expected values in the bulk phases. Those changes were found to be proportional to the interfacial thickness, and they suggested guidelines for minimizing the loss of mass. Moreover, there exists a critical radius below which drops will eventually disappear. With a properly chosen mobility parameter, however, this process will be much slower than the physics of interest and thus has little ill effect on the simulation.

https://doi.org/10.4208/cicp.301110.040811a Published online by Cambridge University Press

In [102], a volume preserving Allen-Cahn type phase equation is used

$$\phi_t+\mathbf{u}\cdot\nabla\phi=\frac{1}{Pe}(-f(\phi)+\epsilon^2\Delta\phi+\xi(t)),$$
$$\frac{d}{dt}\int_\Omega \phi d\mathbf{x}=0,$$

where $\xi(t)$ is the Lagrange multiplier corresponding to the constant volume constraint. One of the reasons for choosing Allen-Cahn rather than Cahn-Hilliard is its numerical treatment is simpler than that of the Cahn-Hilliard type which involves fourth-order differential operators.

2.1.1 Variable density and viscosity

Density and viscosity are linear functions of the phase-field [6, 56]. Let ρ_1 and ρ_2 be the densities of each fluid in the mixture, then the density of the mixture is defined as

$$\rho(c)=\rho_1 c+\rho_2(1-c),\qquad \rho(\phi)=\rho_1\frac{1+\phi}{2}+\rho_2\frac{1-\phi}{2}.$$

Similarly, the viscosity of the mixture is defined as

$$\eta(c)=\eta_1 c+\eta_2(1-c),\qquad \eta(\phi)=\eta_1\frac{1+\phi}{2}+\eta_2\frac{1-\phi}{2}.$$

Then, if we use the linear interpolation, the density and viscosity change across the interface with the same profiles to the scaled phase-field function. In [73], the harmonic interpolation for the variable density and viscosity is used

$$\frac{1}{\rho(\phi)}=\frac{1+\phi}{2\rho_1}+\frac{1-\phi}{2\rho_2},\qquad \frac{1}{\eta(\phi)}=\frac{1+\phi}{2\eta_1}+\frac{1-\phi}{2\eta_2}.$$

For the density, harmonic interpolation is used and linear interpolation is used for viscosity in [54]

$$\frac{1}{\rho(\phi)}=\frac{1+\phi}{2\rho_1}+\frac{1-\phi}{2\rho_2},\qquad \eta(\phi)=\frac{1+\phi}{2}\eta_1+\frac{1-\phi}{2}\eta_2.$$

One of the reasons to choose the harmonic interpolation is that the solution of the Cahn-Hilliard equation does not satisfy the maximal principle [73]. Hence, the linear interpolation cannot be guaranteed to be bounded away from zero. However, due to the L^∞-bound of the solution [17], the harmonic interpolations lead to the desired properties. In Fig. 3, solid and dashed lines represent linear and harmonic interpolations of density, respectively. As we can see from this figure, if the value of c is negative, then the linear interpolated density can be negative which is not physical value. However, if the harmonic interpolation is used, then we always have positive values for density.

https://doi.org/10.4208/cicp.301110.040811a Published online by Cambridge University Press

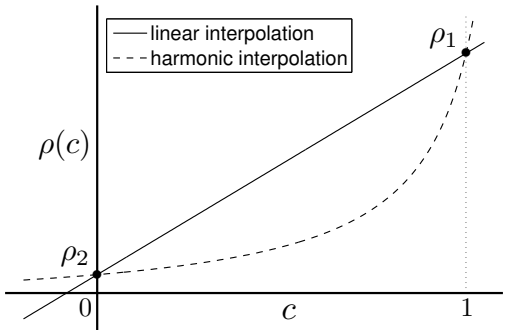

Figure 3: Linear (solid line) and harmonic (dotted line) interpolations of density ρ.

In [30], the applicability of an incompressible diffuse interface model for two-phase incompressible fluid flows with large viscosity and density contrasts was investigated. In [68], authors investigated the long time evolution of the classical Rayleigh-Taylor instability with a phase-field method. They implemented a time-dependent pressure boundary condition through a time-dependent density field at the boundary. Owing to the pressure boundary treatment, they could perform long time evolutions resulting in an equilibrium state.

We note that with the large density ratio, the continuity equation can no longer be reduced to $\nabla\cdot\mathbf{u}$. Therefore, we need to solve $\rho_t+\nabla\cdot(\rho\mathbf{u})$=0.

2.1.2 Surface tension models

A jump condition appears when one investigates Eq. (1.1a) in the neighborhood of the singular surface. This leads to the normal stress condition

$$[\mathbf{n}\cdot(-pI+\eta(\nabla\mathbf{u}+\nabla\mathbf{u}^T))\cdot\mathbf{n}]_\Gamma=\sigma\kappa, \tag{2.11}$$

where $[]_\Gamma$ is a jump across the interface, Γ, and I is the identity matrix. The normal stress condition (2.11) leads to the Laplace's formula for an interface of the principal radii of curvature at a given point of the surface. Let R_1 and R_2 be the principal radii of interface, then the Laplace's formula is given as

$$[p]_\Gamma=\sigma\Big(\frac{1}{R_1}+\frac{1}{R_2}\Big). \tag{2.12}$$

In order to circumvent the problems associated with implementing the Laplace-Young calculation at the exact interface boundary, Brackbill et al. [16] developed a method referred to as the continuum surface force (CSF) method. In the CSF method, the surface tension jump condition is converted into an equivalent singular volume force that is added to the Navier-Stokes equations. Typically, the singular force is smoothed and acts only in a finite transition region across the interface. There are many surface tension

https://doi.org/10.4208/cicp.301110.040811a Published online by Cambridge University Press

models for the phase-field methods

$$\mathbf{SF}_1 = 6\sqrt{2}\epsilon\sigma\nabla\cdot(|\nabla c|^2 I - \nabla c\otimes\nabla c), \quad \mathbf{SF}_2 = \frac{6\sqrt{2}\sigma}{\epsilon}\mu\nabla c, \quad \mathbf{SF}_3 = -\frac{6\sqrt{2}\sigma}{\epsilon}c\nabla\mu, \tag{2.13a}$$

$$\mathbf{SF}_4 = -6\sqrt{2}\epsilon\sigma\nabla\cdot\Big(\frac{\nabla c}{|\nabla c|}\Big)|\nabla c|\nabla c, \qquad \mathbf{SF}_5 = -6\sqrt{2}\epsilon\sigma\nabla\cdot(\nabla c\otimes\nabla c), \tag{2.13b}$$

where the term $\nabla c\otimes\nabla c$ is the usual tensor product, i.e.,

$$\nabla c\otimes\nabla c)_{ij} = \frac{\partial c}{\partial x_i}\frac{\partial c}{\partial x_j}.$$

In [56,69,70,73,74,89], the surface tension formulation $\mathbf{SF}_1$ is used. In [5,6,13,25,43,45,52, 59,66,98,104], $\mathbf{SF}_2$ is used. $\mathbf{SF}_3$ is used in [46–48,63,99]. The surface tension formulation $\mathbf{SF}_4$ allows us to calculate the pressure field directly from the governing equations [56]. In [12,26,86,102,105], $\mathbf{SF}_5$ is used. For more detailed discussions about surface tension models, interested readers are referred to [56].

2.1.3 Contact angle boundary conditions

The spreading of a liquid droplet on a solid surface under capillary action plays an important role in diverse technologies such as inkjet printing. The contact angle is the dihedral angle formed at the interface among three fluid phases (α, β and γ) or between two fluid phases (α and β) and a solid surface γ, as shown in Fig. 4(a) and (b). We shall represent the dihedral angles by θ_α, θ_β, and θ_γ, thus naming them after the phases they contain. At equilibrium, the net force on any element of the three phase lines vanishes. Resolving this force in directions that lie, respectively, along the $\alpha\beta$, $\beta\gamma$, and $\gamma\alpha$ interfaces and are perpendicular to the three phases line, we have

$$\sigma_{\alpha\beta} + \sigma_{\beta\gamma}\cos\theta_\beta + \sigma_{\gamma\alpha}\cos\theta_\alpha = 0, \tag{2.14a}$$

$$\sigma_{\alpha\beta}\cos\theta_\beta + \sigma_{\beta\gamma} + \sigma_{\gamma\alpha}\cos\theta_\gamma = 0, \tag{2.14b}$$

$$\sigma_{\alpha\beta}\cos\theta_\alpha + \sigma_{\beta\gamma}\cos\theta_\gamma + \sigma_{\gamma\alpha} = 0, \tag{2.14c}$$

where $\sigma_{\alpha\beta}$ is the tension of the $\alpha\beta$ interface, etc. [84]. When the γ phase is a solid as shown in Fig. 4(b), the angle θ_γ is π. In this case, the second equation of (2.14) becomes

$$\sigma_{\alpha\beta}\cos\theta_\beta = \sigma_{\gamma\alpha} - \sigma_{\beta\gamma},$$

which is Young's equation [103] and we denote this θ_β by θ.

In the phase-field model, on the domain boundary $\partial\Omega$, we have the following conditions

$$\frac{\partial\phi(\mathbf{x},t)}{\partial n} = -\frac{f_w'(\phi(\mathbf{x},t))}{\epsilon^2}, \quad \mathbf{x}\in\partial\Omega, \quad 0<t\le T, \tag{2.15a}$$

$$\frac{\partial\mu(\mathbf{x},t)}{\partial n} = 0, \tag{2.15b}$$

https://doi.org/10.4208/cicp.301110.040811a Published online by Cambridge University Press

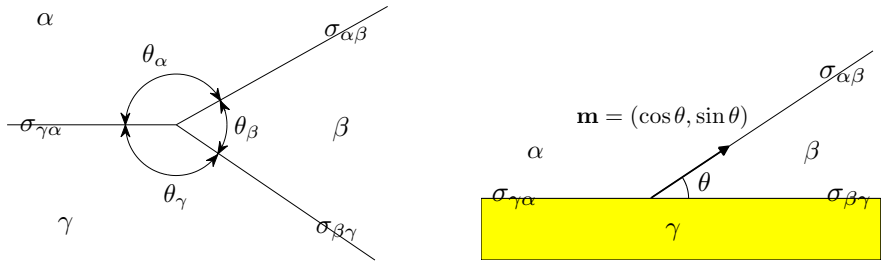

Figure 4: Definitions of dihedral angles at the junctions of three surfaces where three phases meet. (a) α, β, and γ are fluids. (b) α and β are fluids and γ is a solid.

where $f_w(\phi)=\epsilon(\phi^3-3\phi)/(3\sqrt{2})\cos\theta$ is the specific wall free energy, which depends only on the concentration at the solid surface and the contact angle θ [48,54]. This arises from the total Helmholtz free energy functional

$$\mathcal{F}(\phi)=\mathcal{E}(\phi)+\mathcal{W}(\phi)=\int_\Omega\left(F(\phi)+\frac{\epsilon^2}{2}|\nabla\phi|^2\right)d\mathbf{x}+\int_{\partial\Omega}f_w(\phi)ds.$$

The surface integral term $\mathcal{W}(\phi)$ represents the contribution of solid-fluid interactions; it is also used in [54] for diffuse-interface modeling of droplet impacts on solid surfaces. Ding and Spelt [29] proposed a geometric formulation and we briefly describe the geometric formulation: The normal vector to the interface can be written in terms of the gradient of ϕ as $\mathbf{n}_s=\nabla\phi/|\nabla\phi|$. At the contact line, $\mathbf{n}_s$ intersects the solid substrate at an angle of θ, where θ is the contact angle (see Fig. 5). Then, the contact angle can be computed geometrically in terms of ϕ by

$$\tan\left(\frac{\pi}{2}-\theta\right)=\frac{\mathbf{n}\cdot\nabla\phi}{|\nabla\phi-(\mathbf{n}\cdot\nabla\phi)\mathbf{n}|}. \tag{2.16}$$

Eq. (2.16) is referred to as a geometric formulation for the computation of the contact angle θ. For example, to evaluate $\phi_{i,0}$ values, we use the following extrapolation:

$$\phi_{i,0}=\phi_{i,2}-\tan\left(\frac{\pi}{2}-\theta\right)|\phi_{i+1,1}-\phi_{i-1,1}|.$$

Let the phase-field be defined as

$$\phi(x,y)=\tanh\frac{\sin(\theta)x-\cos(\theta)y}{\sqrt{2}\epsilon},$$

which means that the contact angle is θ at the origin. For a contact angle boundary condition, we have $\nabla\phi\cdot\mathbf{m}=0$, where $\mathbf{m}=(\cos(\theta),\sin(\theta))$ is a unit tangent vector to the interface at the contact point and θ is a prescribed contact angle (see Fig. 4(b)). When the contact

https://doi.org/10.4208/cicp.301110.040811a Published online by Cambridge University Press

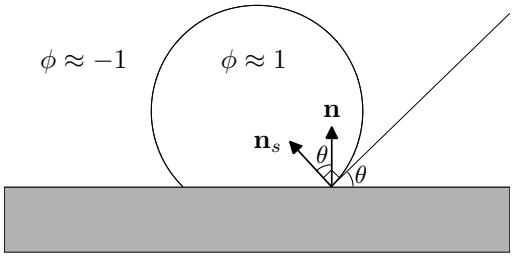

Figure 5: Contact angle θ, unit normal vector $\mathbf{n}$ on the domain boundary, and unit normal vector $\mathbf{n}_s$ on the interface.

angle is $\theta=90^\circ$, we have $\phi_{i,0}^{n+1}=\phi_{i,1}^{n+1}$. When the contact angle is $\theta=45^\circ$, we have

$$\phi_{i,0}^{n+1}=\begin{cases}\phi_{i+1,1}^{n+1}, & \text{if } \phi_{i-1,1}^{n+1}>\phi_{i+1,1}^{n+1},\\ \phi_{i-1,1}^{n+1}, & \text{otherwise.}\end{cases}$$

When the contact angle is $\theta=\tan^{-1}(0.5)(180/\pi)^\circ$, we have

$$\phi_{i,0}^{n+1}=\begin{cases}\phi_{i+2,1}^{n+1}, & \text{if } \phi_{i-1,1}^{n+1}>\phi_{i+1,1}^{n+1},\\ \phi_{i-2,1}^{n+1}, & \text{otherwise.}\end{cases}$$

These interpolations are shown in Fig. 6(a). If the prescribed contact angle is not particular angles ($\theta=90^\circ$, 45°, $\frac{180}{\pi}\tan^{-1}(0.5)^\circ$), then we use an interpolation between the two closest points. For example, when $\theta=60^\circ$, the angle is between $\theta=45^\circ$ and $\theta=90^\circ$, therefore we use $\phi_{i,1}^{n+1}$ and $\phi_{i+1,1}^{n+1}$ to get $\phi_{i,0}^{n+1}$ value

$$\phi_{i,0}^{n+1}=\begin{cases}\left(1-\frac{1}{\sqrt{3}}\right)\phi_{i,1}^{n+1}+\frac{1}{\sqrt{3}}\phi_{i+1,1}^{n+1}, & \text{if } \phi_{i-1,1}^{n+1}>\phi_{i+1,1}^{n+1},\\ \frac{1}{\sqrt{3}}\phi_{i-1,1}^{n+1}+\left(1-\frac{1}{\sqrt{3}}\right)\phi_{i,1}^{n+1}, & \text{otherwise.}\end{cases}$$

This is shown in Fig. 6(b).

In general, when $\theta\neq 0^\circ$, 90° ,180°, the characteristic line is $y=\tan(\theta)x$ and the interpolation position of x-coordinate is $x=h/\tan(\theta)$. We can write x as a sum of an integer part and a fraction part, i.e., $x=k+\alpha$, where k is an integer and $0\leq\alpha<1$. Then the characteristic interpolation is defined as

$$\phi_{i,0}^{n+1}=\begin{cases}(1-\alpha)\phi_{i+k,1}^{n+1}+\alpha\phi_{i+k+1,1}^{n+1}, & \text{if } \phi_{i-1,1}^{n+1}>\phi_{i+1,1}^{n+1},\\ \alpha\phi_{i+k-1,1}^{n+1}+(1-\alpha)\phi_{i+k,1}^{n+1}, & \text{otherwise.}\end{cases}$$

For more detailed discussions about contact angle boundary conditions, interested readers are referred to [67]. In [45], authors combined an operator-splitting scheme for the time-discretization with a finite element space approximation for the system coupling the

https://doi.org/10.4208/cicp.301110.040811a Published online by Cambridge University Press

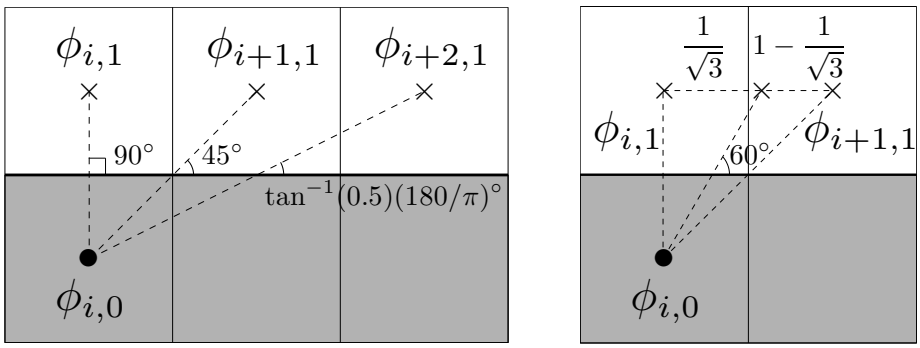

Figure 6: (a) Illustration of the characteristic interpolation stencil for particular contact angles ($\theta=90°$, $45°$, $\tan^{-1}(0.5)(180/\pi)°$) at a domain boundary. (b) Characteristic interpolation stencil for the contact angle $\theta=60°$ at a domain boundary.

Navier-Stokes and Cahn-Hilliard equations modeling the motion of the contact line separating two immiscible incompressible viscous fluids near a solid wall; the combination that they considered allowed large time discretization steps. To treat the Cahn-Hilliard part of the problem, they introduced a least-squares method to overcome the difficulties associated with the nonlinearity and the boundary conditions. The least-squares problem is solved by a conjugate gradient algorithm operating in a well-chosen functional space. Using an energy method, they showed that the scheme has good stability properties.

2.1.4 The Boussinesq approximation

To model mixtures of different densities, authors in [5, 73] used the classical Boussinesq approximation, which is the linear version of all different types of average approaches. The background density can be treated as a constant density and the difference between the actual variable density and the constant will contribute only to the buoyancy force [72]

$$\begin{aligned}
&\rho_*(\mathbf{u}_t+\mathbf{u}\cdot\nabla\mathbf{u})=-\nabla p+\nabla\cdot[\eta(\phi)(\nabla\mathbf{u}+\nabla\mathbf{u}^T)]+\mathbf{SF}+\rho(\phi)\mathbf{g},\\
&\nabla\cdot\mathbf{u}=0,\\
&\phi_t+\mathbf{u}\cdot\nabla\phi=\nabla\cdot(M(\phi)\nabla\mu),\\
&\mu=F'(\phi)-\epsilon^2\Delta\phi,
\end{aligned}$$

where ρ_* is the background density. One of reasons for using the Boussinesq approximation is that it allows for easy calculation of the Navier-Stokes equation. We can write the momentum equation in two-dimensional space as follows:

$$\rho_*(\mathbf{u}_t+\mathbf{u}\cdot\nabla\mathbf{u})=-\nabla(p+\rho_* gy)+\nabla\cdot[\eta(\phi)(\nabla\mathbf{u}+\nabla\mathbf{u}^T)]+\mathbf{SF}+(\rho(\phi)-\rho_*)\mathbf{g}.$$

If we reset the pressure field as $p=p+\rho_* gy$, then the equation becomes

$$\rho_*(\mathbf{u}_t+\mathbf{u}\cdot\nabla\mathbf{u})=-\nabla p+\nabla\cdot[\eta(\phi)(\nabla\mathbf{u}+\nabla\mathbf{u}^T)]+\mathbf{SF}+(\rho(\phi)-\rho_*)\mathbf{g}. \tag{2.17}$$

https://doi.org/10.4208/cicp.301110.040811a Published online by Cambridge University Press

The Boussinesq approximation, Eq. (2.17), is used in [5]. $\rho_* = (\rho_1+\rho_2)/2$ is taken as the mean density in [47]. $\rho_* = \rho_1 (< \rho_2)$ is taken as the mean density in [65]. One advantage of using the Boussinesq approximation is that we solve a constant instead of variable coefficient Poisson equation.

2.1.5 Diffuse-interface simulations of drop coalescence and retraction in viscoelastic fluids

In this section, we consider a diffuse-interface formulation to drop coalescence and retraction involving Newtonian and Oldroyd-*B* fluids

$$\rho(\phi)(\mathbf{u}_t+\mathbf{u}\cdot\nabla\mathbf{u}) = -\nabla p+\nabla\cdot\boldsymbol{\tau}, \tag{2.18a}$$
$$\nabla\cdot\mathbf{u} = 0, \tag{2.18b}$$
$$\phi_t+\mathbf{u}\cdot\nabla\phi = \nabla\cdot(M(\phi)\nabla\mu), \tag{2.18c}$$
$$\mu = F'(\phi)-\epsilon^2\Delta\phi. \tag{2.18d}$$

Adding the interfacial elastic stress, $\lambda\nabla\phi\nabla\phi$ and the proper viscous stress, we obtain the total stress tensor:

$$\boldsymbol{\tau} = \Big(\frac{1-\phi}{2}\mu_n+\frac{1+\phi}{2}\mu_s\Big)(\nabla\mathbf{u}+\nabla\mathbf{u}^T)+\frac{1+\phi}{2}\boldsymbol{\tau}_d+\lambda\nabla\phi\nabla\phi,$$
$$\boldsymbol{\tau}_d+\lambda_H\boldsymbol{\tau}_{d(1)} = \mu_p(\nabla\mathbf{u}+\nabla\mathbf{u}^T),$$

where the subscript $_{(1)}$ denotes the upper convected derivative $\boldsymbol{\tau}_{d(1)} = \partial\boldsymbol{\tau}_d/\partial t+\mathbf{u}\cdot\nabla\boldsymbol{\tau}_d-\nabla\mathbf{u}^T\cdot\boldsymbol{\tau}_d-\boldsymbol{\tau}_d\cdot\nabla\mathbf{u}$, $\lambda_H = \zeta/(4H)$ is the relaxation time, ζ is the friction coefficient between the dumbbell beads and the suspending solvent, and $\mu_p = nkT\lambda_H$ is the polymer viscosity. Please refer to [105, 106] for more details about a diffuse-interface formulation of Newtonian and Oldroyd-*B* fluids.

2.2 A ternary fluid

We next consider a ternary fluid system. The composition of a ternary mixture (*A*, *B*, and *C*) can be mapped onto an equilateral triangle (the Gibbs triangle [82]) as shown in Fig. 7(a). Mixtures with components lying on lines parallel to $\overline{BC}$ contain the same percentage of *A*, those with lines parallel to $\overline{AC}$ have the same percentage of *B* concentration, and analogously for the *C* concentration. In Fig. 7(a), the mixture at the position marked "$\circ$" contains 60%*A*, 10%*B* and 30%*C*.

Let $\mathbf{c} = (c_1, c_2)$ be the phase variable (i.e., concentrations of component A and component B). Since $c_1+c_2+c_3 = 1$ we only need to solve the equations with c_1 and c_2. For three immiscible fluids, the free energy can be modeled by $F(\mathbf{c}) = \frac{1}{4}\sum_{i<j}^{3} c_i^2 c_j^2$. The contours of the free energy $F(\mathbf{c})$ projected onto the Gibbs triangle are shown in Fig. 7(b). Note the energy minima are at the three vertices and the maximum is at the center. The dimensional

https://doi.org/10.4208/cicp.301110.040811a Published online by Cambridge University Press

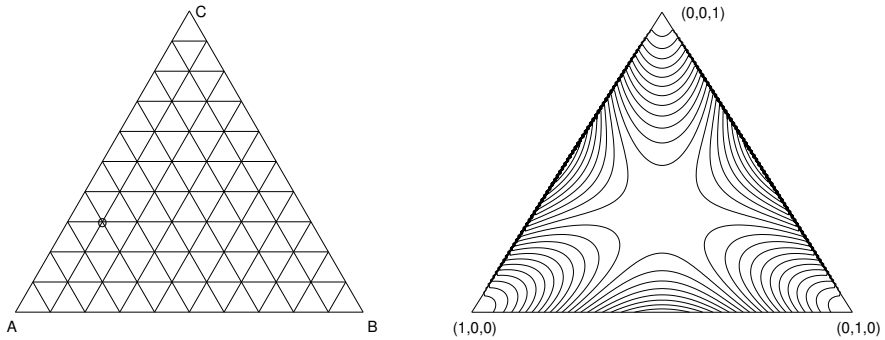

(a) (b)

Figure 7: (a) Gibbs triangle. (b) Contour plot of the free energy $F(\mathbf{c})$.

ternary phase-field system [59] is as follows:

$$\rho(\mathbf{u}_t+\mathbf{u}\cdot\nabla\mathbf{u})=-\nabla p+\nabla\cdot[\eta(\mathbf{c})(\nabla\mathbf{u}+\nabla\mathbf{u}^T)]+\mathbf{SF}+\rho\mathbf{g}, \tag{2.19a}$$

$$\nabla\cdot\mathbf{u}=0, \tag{2.19b}$$

$$\frac{\partial c_1}{\partial t}+\mathbf{u}\cdot\nabla c_1=\nabla\cdot(M(\mathbf{c})\nabla\mu_1), \tag{2.19c}$$

$$\frac{\partial c_2}{\partial t}+\mathbf{u}\cdot\nabla c_2=\nabla\cdot(M(\mathbf{c})\nabla\mu_2), \tag{2.19d}$$

$$\mu_1=\frac{\partial F(\mathbf{c})}{\partial c_1}-c_1c_2(1-c_1-c_2)-\epsilon^2\Delta c_1, \tag{2.19e}$$

$$\mu_2=\frac{\partial F(\mathbf{c})}{\partial c_2}-c_1c_2(1-c_1-c_2)-\epsilon^2\Delta c_2. \tag{2.19f}$$

In [15], the advective Cahn-Hilliard equations are given as the following form:

$$\frac{\partial c_i}{\partial t}+\mathbf{u}\cdot\nabla c_i=\nabla\cdot\Big(\frac{M_0}{\sigma_i}\nabla\mu_i\Big),\quad \text{for } i=1,2,3,$$
$$\mu_i=\frac{4\sigma_T}{\epsilon}\sum_{j\neq i}\frac{1}{\sigma_j}\Big(\frac{\partial F(\mathbf{c})}{\partial c_i}-\frac{\partial F(\mathbf{c})}{\partial c_j}\Big)-\frac{3}{4}\epsilon\sigma_i\Delta c_i,$$

where M_0 is the mobility, the coefficient σ_T is defined by $3/\sigma_T=\sum_{i=1}^{3}1/\sigma_i$, and $\sigma_i+\sigma_j=2\sigma_{ij}$, for $i<j$. The bulk free energy potential is defined as $F(\mathbf{c})=\sum_{i<j}^{3}\sigma_{ij}c_i^2c_j^2+\sum_{i=1}^{3}\sigma_ic_i$.

In three component fluids [14, 58, 64, 88], phase specific decomposition surface forces are used. We decompose the given physical surface tension coefficients, σ_{ij}, of the interface Γ_{ij} between fluid $i(\Omega_i)$ and fluid $j(\Omega_j)$ (see Fig. 8(a)) into the phase specific surface tension coefficients σ_1, σ_2, and σ_3 such that:

$$\sigma_{12}=\sigma_1+\sigma_2,\qquad \sigma_{13}=\sigma_1+\sigma_3,\qquad \sigma_{23}=\sigma_2+\sigma_3.$$

https://doi.org/10.4208/cicp.301110.040811a Published online by Cambridge University Press

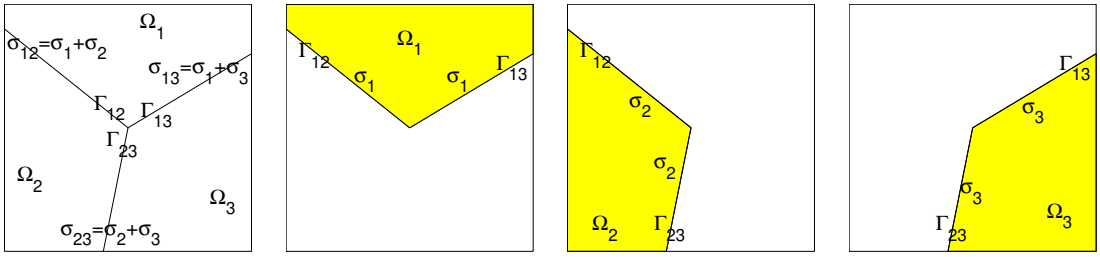

Figure 8: Schematic of a domain. (a) σ_{ij} denotes the surface tension coefficient of the interface Γ_{ij} of fluids Ω_i and Ω_j. (b) Phase specific surface tension coefficient, σ_1, on interfaces, Γ_{12} and Γ_{13}. (c) and (d) are similarly defined.

The decomposition is uniquely defined as $\sigma_1=(\sigma_{12}-\sigma_{23}+\sigma_{13})/2$, $\sigma_2=(\sigma_{12}+\sigma_{23}-\sigma_{13})/2$, and $\sigma_3=(-\sigma_{12}+\sigma_{23}+\sigma_{13})/2$ (see Fig. 8(b), (c), and (d)). Then the continuous surface tension force is defined as

$$\mathbf{SF}=\sum_{k=1}^{3}\mathbf{SF}_k=\sum_{k=1}^{3}\sigma_k\kappa(c_k)\mathbf{n}(c_k)\delta(c_k),$$

where $\kappa(c_k)=\nabla\cdot(\nabla c_k/|\nabla c_k|)$, $\mathbf{n}(c_k)$, and $\delta(c_k)$ are the curvature, the unit normal vector, and the smoothed Dirac delta function of the k-th fluid interface, respectively. A capillary force,

$$\mathbf{SF}=\mu_1\nabla c_1+\mu_2\nabla c_2+\mu_3\nabla c_3=\sum_{i=1}^{3}\mu_i\nabla c_i$$

is considered in the momentum balance. For variable density and viscosity, the following interpolations are used

$$\rho(c_1,c_2)=(\rho_1-\rho_3)H_\epsilon(c_1-0.5)+(\rho_2-\rho_3)H_\epsilon(c_2-0.5)+\rho_3, \tag{2.20a}$$
$$\eta(c_1,c_2)=(\eta_1-\eta_3)H_\epsilon(c_1-0.5)+(\eta_2-\eta_3)H_\epsilon(c_2-0.5)+\eta_3, \tag{2.20b}$$

where H_ϵ is a smooth approximation of a Heaviside function. Contrary to the arithmetic or harmonic averages used in the literature, these relationships (2.20a) and (2.20b) enable one to preserve the values ρ_i and η_i in phase i even though c_i is not exactly 1 due to numerical errors [15].

2.3 A diffuse-interface method for two-phase flows with soluble surfactants

In [93], a method was presented to solve two-phase problems involving soluble surfactants. The incompressible Navier-Stokes equations are solved along with equations for the bulk and interfacial surfactant concentrations. A nonlinear equation of state is used to relate the surface tension to the interfacial surfactant concentration. Results were

https://doi.org/10.4208/cicp.301110.040811a Published online by Cambridge University Press

presented for a drop in shear flow in both 2D and 3D, and the effect of solubility was discussed. Let a phase-field function c, which is 1 in Ω_1 and 0 in Ω_2, then we define $\Gamma(t)=\{\mathbf{x}\in\Omega|c(\mathbf{x},t)=1/2\}$

$$\frac{\partial c}{\partial t}+\nabla\cdot(c\mathbf{u})=\nabla\cdot(M(c)\nabla\mu), \tag{2.21a}$$

$$\mu=F'(c)-\epsilon^2\Delta c, \tag{2.21b}$$

where $M=\sqrt{c^2(1-c)^2}$ is a mobility function. Let f be the dimensionless surfactant concentration, which gives the dimensionless surface tension

$$\sigma(f)=1+\beta\ln(1-xf), \tag{2.22}$$

where β is the elasticity number and x is the dimensionless surfactant coverage. Let F be the dimensionless surfactant concentration in the bulk fluid

$$\frac{\partial}{\partial t}(f\delta_\Gamma)+\nabla\cdot(f\delta_\Gamma\mathbf{u})=\frac{1}{Pe_f}\nabla\cdot(\delta_\Gamma\nabla f)+\delta_\Gamma j, \tag{2.23a}$$

$$\frac{\partial}{\partial t}(\chi F)+\nabla\cdot(\chi F\mathbf{u})=\frac{1}{Pe_F}\nabla\cdot(\chi\nabla F)-h\delta_\Gamma j, \tag{2.23b}$$

where Pe_f is the surface Peclet number, Pe_F is the bulk Peclet number, and h is the adsorption depth. The dimensionless source term, j, is given by

$$j(F,f)=\mathrm{Bi}\left[kF_s\left(\frac{1}{x}-f\right)-f\right]. \tag{2.24}$$

The dimensionless parameters are Bi (Biot number) and k (adsorption number). For the regularized surface delta function and characteristic function, $\delta_\Gamma=3\sqrt{2}c^2(1-c)^2/\epsilon$ and $\chi=1-c$ were used, respectively. For more details about a diffuse-interface method for two-phase flows with soluble surfactants, please refer to [93].

2.4 More than a ternary fluid

It has been noted by several authors [14, 64] that in the quaternary case, the use of phase specific decomposition cannot be used. This is because the decomposition generates a system of over-determined equations and a solution may not exist. In fact, in [88], "$n>2$" only means "$n=3$". Here n represents the number of fluid components. For example, if $n=4$, then given the physical surface tension coefficients σ_{ij} of the interface Γ_{ij} between fluid i and fluid j, we may consider a linear system of six equations to determine the four unknowns σ_1, σ_2, σ_3 and σ_4:

$$\sigma_{12}=\sigma_1+\sigma_2, \qquad \sigma_{13}=\sigma_1+\sigma_3, \qquad \sigma_{14}=\sigma_1+\sigma_4, \tag{2.25a}$$

$$\sigma_{23}=\sigma_2+\sigma_3, \qquad \sigma_{24}=\sigma_2+\sigma_4, \qquad \sigma_{34}=\sigma_3+\sigma_4. \tag{2.25b}$$

https://doi.org/10.4208/cicp.301110.040811a Published online by Cambridge University Press

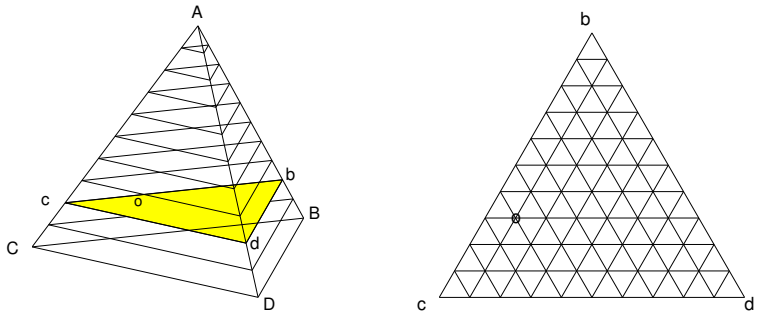

(a) (b)

Figure 9: (a) Gibbs tetrahedron. (b) A slice plane parallel to the BCD triangle.

But the above systems of equations are over-determined equations; therefore, it is possible that there is no solution. In order to ensure that these equations possess a unique solution, some restrictions must be imposed on σ_{ij}. Note that, in general, for an n component immiscible fluid system, there are $n(n-1)/2$ possible interfaces and $n(n-1)/2>n$ for $n\geq 4$. This implies that we have more equations than unknowns.

The composition of a quaternary mixture (A, B, C and D) can be mapped onto an equilateral tetrahedron (the Gibbs simplex [82]) whose corners represent a 100% concentration of A, B, C or D as shown in Fig. 9(a). Mixtures with components lying on planes parallel to the triangle, ΔBCD, contain the same percentage of A; those with planes parallel to the triangle, ΔCDA, have the same percentage of B concentration; analogously, the same relationships exist for the C and the D concentrations. In Fig. 9, the mixture at the position marked "$\circ$" contains 20%A, 24%B, 48%C, and 8%D.

Let $\mathbf{c}=(c_1,c_2,c_3,c_4)$ be the phase variables (i.e., the mole fractions of A, B, C, and D, respectively). Thus, admissible states will belong to the Gibbs tetrahedron

$$GT:=\left\{\mathbf{c}\in\mathbb{R}^4\middle|\sum_{i=1}^{4}c_i=1,\quad 0\leq c_i\leq 1\right\}. \tag{2.26}$$

Without the loss of generalities, we postulate that the free energy can be written as follows

$$\mathcal{F}=\int_\Omega\left[F(\mathbf{c})+\frac{\epsilon^2}{2}\sum_{i=1}^{4}|\nabla c_i|^2\right]d\mathbf{x},$$

where $F(\mathbf{c})=0.25\sum_{i=1}^{4}c_i^2(1-c_i)^2$, ϵ is a positive constant, and Ω is an open bounded subset of $\mathbb{R}^n$ $(n=2,3)$ occupied by the system. The time evolution of $\mathbf{c}$ is governed by the gradient of the energy with respect to the H^{-1} inner product under the additional constraint (2.26). This constraint has to hold everywhere at any time. In order to ensure this last constraint, we use a variable Lagrangian multiplier $\beta(\mathbf{c})$ [38]. The time dependence of c_i is given by the following advective Cahn-Hilliard equation for describing each phase

https://doi.org/10.4208/cicp.301110.040811a Published online by Cambridge University Press

convection:

$$\frac{\partial c_i}{\partial t}+\mathbf{u}\cdot\nabla c_i = M\Delta\mu_i, \quad i=1,2,3,4, \tag{2.27a}$$

$$\mu_i = \frac{\partial F(\mathbf{c})}{\partial c_i}-\epsilon^2\Delta c_i+\beta(\mathbf{c}), \tag{2.27b}$$

where $\mathbf{u}$ is the fluid velocity and M is the mobility. To calculate $\beta(\mathbf{c})$, we write an equation satisfied by $S=c_1+c_2+c_3+c_4$ and we want $S\equiv 1$ to be a solution to the following equation

$$\frac{\partial S}{\partial t}+\mathbf{u}\cdot\nabla S = M\Delta\Big(\sum_{i=1}^{4}\frac{\partial F}{\partial c_i}-\epsilon^2\Delta S+4\beta(\mathbf{c})\Big),$$

where we got this from the summation of Eqs. (2.27a) and (2.27b) from $i=1$ to 4. Therefore, $\beta(\mathbf{c})=-0.25\sum_{i=1}^{4}\partial F/\partial c_i$. For the sake of simplicity, we consider a system of four immiscible fluids where the densities of all fluids are assumed to be equal. The variable density can be defined as $\rho(\mathbf{c})=(\sum_{i=1}^{4}c_i/\rho_i)^{-1}$ and ρ_i is the i-th fluid density [64]. The fluids are incompressible and are governed by the Navier-Stokes-Cahn-Hilliard equations [6, 14, 25, 48, 56, 58, 64]

$$\rho\Big(\frac{\partial \mathbf{u}}{\partial t}+\mathbf{u}\cdot\nabla\mathbf{u}\Big) = -\nabla p+\nabla\cdot[\eta(\mathbf{c})(\nabla\mathbf{u}+\nabla\mathbf{u}^T)]+\mathbf{SF}+\rho\mathbf{g}, \tag{2.28a}$$

$$\nabla\cdot\mathbf{u}=0, \tag{2.28b}$$

$$\frac{\partial \mathbf{c}}{\partial t}+\mathbf{u}\cdot\nabla\mathbf{c} = M\Delta\boldsymbol{\mu}, \tag{2.28c}$$

$$\boldsymbol{\mu} = \mathbf{f}(\mathbf{c})-\epsilon^2\Delta\mathbf{c}, \tag{2.28d}$$

where p is the pressure, $\eta(\mathbf{c})=(\sum_{i=1}^{4}c_i/\eta_i)^{-1}$ is the variable viscosity, $\mathbf{SF}$ is the surface tension force, and $\mathbf{f}(\mathbf{c})=(\partial F/\partial c_1+\beta(\mathbf{c}),\ \partial F/\partial c_2+\beta(\mathbf{c}),\ \partial F/\partial c_3+\beta(\mathbf{c}),\ \partial F/\partial c_4+\beta(\mathbf{c}))$. To avoid the solvability problem imposed by the over-determined system (2.25a), a generalized continuous surface tension force formulation is proposed [60]

$$\begin{aligned}\mathbf{SF}(\mathbf{c}) = &\frac{\sigma_{12}}{2}[\mathbf{sf}(c_1)+\mathbf{sf}(c_2)]\delta(c_1,c_2)+\frac{\sigma_{13}}{2}[\mathbf{sf}(c_1)+\mathbf{sf}(c_3)]\delta(c_1,c_3)\\ &+\frac{\sigma_{14}}{2}[\mathbf{sf}(c_1)+\mathbf{sf}(c_4)]\delta(c_1,c_4)+\frac{\sigma_{23}}{2}[\mathbf{sf}(c_2)+\mathbf{sf}(c_3)]\delta(c_2,c_3)\\ &+\frac{\sigma_{24}}{2}[\mathbf{sf}(c_2)+\mathbf{sf}(c_4)]\delta(c_2,c_4)+\frac{\sigma_{34}}{2}[\mathbf{sf}(c_3)+\mathbf{sf}(c_4)]\delta(c_3,c_4),\end{aligned}$$

where $\mathbf{sf}(c_i)=-6\sqrt{2}\epsilon\nabla\cdot(\nabla c_i/|\nabla c_i|)|\nabla c_i|\nabla c_i$ and $\delta(c_i,c_j)=5c_ic_j$.

In Fig. 10, the dotted line is an equilibrium concentration field $c=0.5(1+\tanh(x/(2\sqrt{2}\epsilon)))$, the dash-dot line is the Dirac delta function $6\sqrt{2}\epsilon c_x^2$ in [56], and the solid line is the new Dirac delta function, $30\sqrt{2}\epsilon c(1-c)c_x^2$; here, $\epsilon=0.1$. We note that the new smoothed Dirac delta function, $5\alpha\epsilon c(1-c)|\nabla c|^2$, allows us to model any number of

https://doi.org/10.4208/cicp.301110.040811a Published online by Cambridge University Press

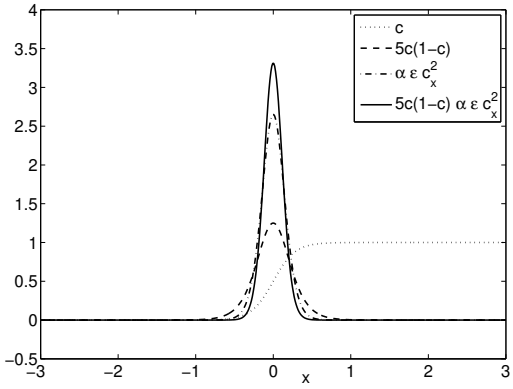

Figure 10: The dotted line represents an equilibrium concentration field $c=0.5(1+\tanh(x/(2\sqrt{2}\epsilon)))$; the dash-dot line is the Dirac delta function $6\sqrt{2}\epsilon c_x^2$; and the solid line is the new Dirac delta function, $30\sqrt{2}\epsilon c(1-c)c_x^2$. $\epsilon=0.1$.

multi-component (more than three) fluid flows. Here $\alpha=6\sqrt{2}$. In general, for the interface between fluid i and fluid j, we have

$$\int_{-\infty}^{\infty} 15\sqrt{2}\epsilon c_i c_j(|\nabla c_i|^2+|\nabla c_j|^2)dx=1,$$

where the integration is taken across the interface. In general, for N component fluids, the surface tension force formulation is

$$\mathbf{SF}(\mathbf{c})=\sum_{i=1}^{N-1}\Big(\sum_{j=i+1}^{N}\frac{\sigma_{ij}}{2}[\mathbf{sf}(c_i)+\mathbf{sf}(c_j)]\delta(c_i,c_j)\Big).$$

2.5 Nondimensionalization

To restate the dimensional NSCH system in dimensionless form, we define the dimensionless variables as

$$x'=\frac{x}{L_c},\quad \mathbf{u}'=\frac{\mathbf{u}}{U_c},\quad t'=\frac{tU_c}{L_c},\quad p'=\frac{p}{\rho_c U_c^2},\quad \mathbf{g}'=\frac{\mathbf{g}}{g},\quad \rho'=\frac{\rho}{\rho_c},\quad \mu'=\frac{\mu}{\mu_c},$$

where L_c, U_c, and ρ_c are the characteristic length, velocity, and density, respectively. g is the gravitational acceleration. Substituting these variables into the governing Eqs. (2.10a)-(2.10d), we have

$$\rho'(\mathbf{u}'_{t'}+\mathbf{u}'\cdot\nabla'\mathbf{u}')=-\nabla' p'+\frac{\eta}{\rho_c U_c L_c}\Delta'\mathbf{u}'-\frac{3\sqrt{2}\sigma\epsilon}{4\rho_c L_c U_c^2}\nabla'\cdot\Big(\frac{\nabla'\phi}{|\nabla'\phi|}\Big)|\nabla'\phi|\nabla'\phi+\frac{gL_c}{U_c^2}\rho'\mathbf{g}', \tag{2.29a}$$

$$\nabla'\cdot\mathbf{u}'=0, \tag{2.29b}$$

$$\phi_{t'}+\nabla'\cdot(\phi\mathbf{u}')=\frac{M\mu_c}{U_c L_c}\Delta'\mu', \tag{2.29c}$$

$$\mu'=\phi^3-\phi-\frac{\epsilon^2}{L_c^2}\Delta'\phi. \tag{2.29d}$$

https://doi.org/10.4208/cicp.301110.040811a Published online by Cambridge University Press

Dropping the primes and resetting $\epsilon^2=\epsilon^2/L_c^2$, Eqs. (2.29a)-(2.29d) become

$$\rho(\mathbf{u}_t+\mathbf{u}\cdot\nabla\mathbf{u})=-\nabla p+\frac{1}{Re}\Delta\mathbf{u}, \tag{2.30a}$$

$$\nabla\cdot\mathbf{u}=0, \tag{2.30b}$$

$$\phi_t+\nabla\cdot(\phi\mathbf{u})=\frac{1}{Pe}\Delta\mu, \tag{2.30c}$$

$$\mu=\phi^3-\phi-\epsilon^2\Delta\phi, \tag{2.30d}$$

where $\mathbf{SF}=-0.75\sqrt{2}\epsilon\nabla\cdot(\nabla\phi/|\nabla\phi|)|\nabla\phi|\nabla\phi$. The dimensionless physical parameters are the Reynolds number, Re, Weber number, We, Froude number, Fr, and Peclet number, Pe, given by

$$Re=\frac{\rho_c U_c L_c}{\eta},\qquad We=\frac{\rho_c L_c U_c^2}{\sigma},\qquad Fr=\frac{U_c^2}{gL_c},\qquad Pe=\frac{U_c L_c}{M\mu_c}.$$

3 Numerical methods

The Fourier-spectral method for Navier-Stokes and Cahn-Hilliard system was used in [73]. Many numerical methods for Navier-Stokes and Cahn-Hilliard system consist of decoupled solutions of the Navier-Stokes equation and the Cahn-Hilliard equation. Therefore, in the following subsections we will describe each numerical solution separately.

3.1 Navier-Stokes solver

In principle, we can use most of numerical solutions for the Navier-Stokes equations in conjunction with the Cahn-Hilliard equations. Examples are the second-order projection method for the incompressible Navier-Stokes equations [9] in [56, 64], the numerical method for solving incompressible viscous flow problems [27] in [59, 60, 68], and high-order splitting methods for the incompressible Navier-Stokes equations [51] in [6].

For completeness of exposition we describe one of simplest numerical solutions of the Navier-Stokes equations. The simultaneous solution of the large number of discrete equations arising from Eqs. (2.10a) and (2.10b) is very costly, especially in three spatial dimensions [71]. An efficient approximation can be obtained by decoupling the solution of the momentum equations from the solution of the continuity equation by a projection method [9, 27]. We will focus on describing the idea in two-dimensions. A staggered marker-and-cell (MAC) mesh of Harlow and Welch [44] is used in which pressure and phase fields are stored at cell centers and velocities at cell interfaces (see Fig. 11).

Let a computational domain be partitioned in Cartesian geometry into a uniform mesh with mesh spacing h. The center of each cell, Ω_{ij}, is located at $(x_i,y_j)=((i-0.5)h,(j-0.5)h)$ for $i=1,\cdots,N_x$ and $j=1,\cdots,N_y$. N_x and N_y are the numbers of cells in the x and y

https://doi.org/10.4208/cicp.301110.040811a Published online by Cambridge University Press

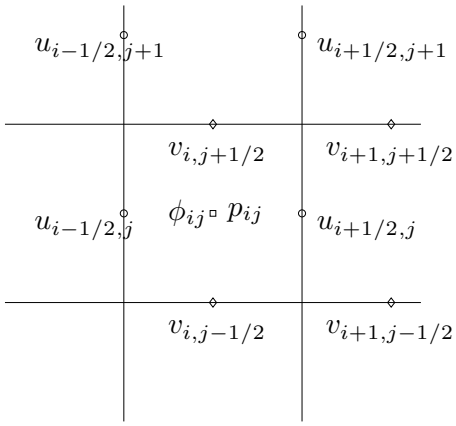

Figure 11: Velocities are defined at cell boundaries while the pressure and phase field are defined at the cell centers.

directions, respectively. The cell vertices are located at $(x_{i+1/2},y_{j+1/2})=(ih,jh)$. At the beginning of each time step, given $\mathbf{u}^n$ and ϕ^n, we want to find $\mathbf{u}^{n+1}$, ϕ^{n+1}, and p^{n+1} which solve the following temporal discretization of the dimensionless form of Eqs. (2.30a)-(2.30d) of motion:

$$\rho^n\frac{\mathbf{u}^{n+1}-\mathbf{u}^n}{\Delta t}=-\rho^n(\mathbf{u}\cdot\nabla_d\mathbf{u})^n-\nabla_d p^{n+1}+\frac{1}{Re}\Delta_d\mathbf{u}^n+\frac{1}{We}\mathbf{SF}^n+\frac{\rho^n}{Fr}\mathbf{g}, \tag{3.1a}$$

$$\nabla_d\cdot\mathbf{u}^{n+1}=0, \tag{3.1b}$$

$$\frac{\phi^{n+1}-\phi^n}{\Delta t}=\frac{1}{Pe}\Delta_d\nu^{n+1}-\frac{1}{Pe}\Delta_d\phi^n-\nabla_d\cdot(\phi\mathbf{u})^n, \tag{3.1c}$$

$$\nu^{n+1}=(\phi^{n+1})^3-\epsilon^2\Delta_d\phi^{n+1}, \tag{3.1d}$$

where $\rho^n=\rho(\phi^n)$ and $\mathbf{g}=(0,-1)$. The outline of the main procedures in one time step follows:

Step 1. Initialize $\mathbf{u}^0$ to be the divergence-free velocity field and ϕ^0.

Step 2. Solve an intermediate velocity field, $\tilde{\mathbf{u}}$, which generally does not satisfy the incompressible condition, without the pressure gradient term,

$$\frac{\tilde{\mathbf{u}}-\mathbf{u}^n}{\Delta t}=-\mathbf{u}^n\cdot\nabla_d\mathbf{u}^n+\frac{1}{\rho^n Re}\Delta_d\mathbf{u}^n+\frac{1}{\rho^n We}\mathbf{SF}^n+\frac{1}{Fr}\mathbf{g}.$$

The resulting finite difference equations are written out explicitly. They take the form

$$\begin{aligned}\tilde{u}_{i+\frac{1}{2},j}=&u^n_{i+\frac{1}{2},j}-\Delta t(uu_x+vu_y)^n_{i+\frac{1}{2},j}+\frac{\Delta t}{\rho^n_{i+\frac{1}{2},j}We}SF^{x-edge}_{i+\frac{1}{2},j}\\&+\frac{\Delta t}{h^2\rho^n_{i+\frac{1}{2},j}Re}\left(u^n_{i+\frac{3}{2},j}+u^n_{i-\frac{1}{2},j}-4u^n_{i+\frac{1}{2},j}+u^n_{i+\frac{1}{2},j+1}+u^n_{i+\frac{1}{2},j-1}\right),\end{aligned} \tag{3.2a}$$

https://doi.org/10.4208/cicp.301110.040811a Published online by Cambridge University Press

$$\tilde{v}_{i,j+\frac{1}{2}} = v^n_{i,j+\frac{1}{2}} - \Delta t(uv_x + vv_y)^n_{i,j+\frac{1}{2}} + \frac{\Delta t}{\rho^n_{i,j+\frac{1}{2}} We} SF^{y-edge}_{i,j+\frac{1}{2}} - \frac{\Delta t}{Fr} + \frac{\Delta t}{h^2 \rho^n_{i,j+\frac{1}{2}} Re}\left(v^n_{i+1,j+\frac{1}{2}} + v^n_{i-1,j+\frac{1}{2},j} - 4v^n_{i,j+\frac{1}{2}} + v^n_{i,j+\frac{3}{2}} + v^n_{i,j-\frac{1}{2}}\right), \tag{3.2b}$$

where the advection terms, $(uu_x + vu_y)^n_{i+1/2,j}$ and $(uv_x + vv_y)^n_{i,j+1/2}$, are defined by

$$(uu_x + vu_y)^n_{i+\frac{1}{2},j} = u^n_{i+\frac{1}{2},j}\bar{u}^n_{x_{i+\frac{1}{2},j}} + \frac{v^n_{i,j-\frac{1}{2}} + v^n_{i+1,j-\frac{1}{2}} + v^n_{i,j+\frac{1}{2}} + v^n_{i+1,j+\frac{1}{2}}}{4}\bar{u}^n_{y_{i+\frac{1}{2},j}},$$
$$(uv_x + vv_y)^n_{i,j+\frac{1}{2}} = \frac{u^n_{i-\frac{1}{2},j} + u^n_{i-\frac{1}{2},j+1} + u^n_{i+\frac{1}{2},j} + u^n_{i+\frac{1}{2},j+1}}{4}\bar{v}^n_{x_{i,j+\frac{1}{2}}} + v^n_{i,j+\frac{1}{2}}\bar{v}^n_{y_{i,j+\frac{1}{2}}}.$$

The values $\bar{u}^n_{x_{i+1/2,j}}$ and $\bar{u}^n_{y_{i+1/2,j}}$ are computed using the upwind procedure. The procedure is

$$\bar{u}^n_{x_{i+\frac{1}{2},j}} = \begin{cases} \dfrac{u^n_{i+\frac{1}{2},j} - u^n_{i-\frac{1}{2},j}}{h}, & \text{if } u^n_{i+\frac{1}{2},j} > 0, \\ \dfrac{u^n_{i+\frac{3}{2},j} - u^n_{i+\frac{1}{2},j}}{h}, & \text{otherwise} \end{cases}$$

and

$$\bar{u}^n_{y_{i+\frac{1}{2},j}} = \begin{cases} \dfrac{u^n_{i+\frac{1}{2},j} - u^n_{i+\frac{1}{2},j-1}}{h}, & \text{if } v^n_{i,j-\frac{1}{2}} + v^n_{i+1,j-\frac{1}{2}} + v^n_{i,j+\frac{1}{2}} + v^n_{i+1,j+\frac{1}{2}} > 0, \\ \dfrac{u^n_{i+\frac{1}{2},j+1} - u^n_{i+\frac{1}{2},j}}{h}, & \text{otherwise.} \end{cases}$$

The quantities $\bar{v}^n_{x_{i,j+1/2}}$ and $\bar{v}^n_{y_{i,j+1/2}}$ are computed in a similar manner. The surface tension force terms, $SF^{x-edge}_{i+1/2,j}$ and $SF^{y-edge}_{i,j+1/2}$, are computed using the procedure derived in [59]. Then, we solve the following equations for the advanced pressure field at the $(n+1)$ time step

$$\frac{\mathbf{u}^{n+1} - \tilde{\mathbf{u}}}{\Delta t} = -\frac{1}{\rho^n}\nabla_d p^{n+1}, \tag{3.3a}$$
$$\nabla_d \cdot \mathbf{u}^{n+1} = 0. \tag{3.3b}$$

With application of the divergence operator to Eq. (3.3a), we find that the Poisson equation for the pressure at the advanced time $(n+1)$ is

$$\nabla_d \cdot \left(\frac{1}{\rho^n}\nabla_d p^{n+1}\right) = \frac{1}{\Delta t}\nabla_d \cdot \tilde{\mathbf{u}}, \tag{3.4}$$

https://doi.org/10.4208/cicp.301110.040811a Published online by Cambridge University Press

where we have made use of the Eq. (3.3b) and the terms are defined as follows:

$$\nabla_d\cdot\Big(\frac{1}{\rho^n}\nabla_d p_{ij}^{n+1}\Big)=\frac{\frac{1}{\rho^n_{i+\frac12,j}}p^{n+1}_{i+1,j}+\frac{1}{\rho^n_{i-\frac12,j}}p^{n+1}_{i-1,j}+\frac{1}{\rho^n_{i,j+\frac12}}p^{n+1}_{i,j+1}+\frac{1}{\rho^n_{i,j-\frac12}}p^{n+1}_{i,j-1}}{h^2}$$
$$-\frac{\frac{1}{\rho^n_{i+\frac12,j}}+\frac{1}{\rho^n_{i-\frac12,j}}+\frac{1}{\rho^n_{i,j+\frac12}}+\frac{1}{\rho^n_{i,j-\frac12}}}{h^2}p_{ij}^{n+1},$$
$$\nabla_d\cdot\tilde{\mathbf{u}}_{ij}=\frac{\tilde u_{i+\frac12,j}-\tilde u_{i-\frac12,j}}{h}+\frac{\tilde v_{i,j+\frac12}-\tilde v_{i,j-\frac12}}{h},$$

where $\rho^n_{i+1/2,j}=(\rho^n_{ij}+\rho^n_{i+1,j})/2$ and the other terms are similarly defined. The boundary condition for the pressure is

$$\mathbf{n}\cdot\nabla_d p^{n+1}=\mathbf{n}\cdot\Big(-\rho^n\frac{\mathbf{u}^{n+1}-\mathbf{u}^n}{\Delta t}-\rho^n(\mathbf{u}\cdot\nabla_d\mathbf{u})^n+\frac{1}{Re}\Delta_d\mathbf{u}^n+\frac{1}{We}\mathbf{SF}^n+\frac{\rho^n}{Fr}\mathbf{g}\Big),$$

where $\mathbf{n}$ is the unit normal vector to the domain boundary. In our application of the phase-field to the Rayleigh-Taylor instability, we will use a periodic boundary condition to vertical boundaries and no slip boundary condition to the top and bottom domain. Therefore,

$$\mathbf{n}\cdot\nabla_d p^{n+1}=\mathbf{n}\cdot\Big(\frac{1}{We}\mathbf{SF}^n+\frac{\rho^n}{Fr}\mathbf{g}\Big). \tag{3.5}$$

The resulting linear system of Eq. (3.4) is solved using a multigrid method [95], specifically, V-cycles with a Gauss-Seidel relaxation. Then the divergence-free normal velocities u^{n+1} and v^{n+1} are defined by

$$\mathbf{u}^{n+1}=\tilde{\mathbf{u}}-\frac{\Delta t}{\rho^n}\nabla_d p^{n+1},$$

i.e.,

$$u^{n+1}_{i+\frac12,j}=\tilde u_{i+\frac12,j}-\frac{\Delta t}{\rho^n_{i+\frac12,j}h}(p_{i+1,j}-p_{ij}),\qquad v^{n+1}_{i,j+\frac12}=\tilde v_{i,j+\frac12}-\frac{\Delta t}{\rho^n_{i,j+\frac12}h}(p_{i,j+1}-p_{ij}).$$

We implement the unconditionally gradient stable scheme in Eqs. (3.1c)-(3.1d) with a nonlinear multigrid method. For a detailed description of the numerical method used in solving these equations, please refer to [56, 61]. If mass conservation is an important factor, we use a conservative discretization of the convective part of the phase-field equation (3.1c)

$$((\phi u)_x+(\phi v)_y)^n_{ij}=\frac{u^n_{i+\frac12,j}(\phi^n_{i+1,j}+\phi^n_{ij})-u^n_{i-\frac12,j}(\phi^n_{ij}+\phi^n_{i-1,j})}{2h}$$
$$+\frac{v^n_{i,j+\frac12}(\phi^n_{i,j+1}+\phi^n_{ij})-u^n_{i,j-\frac12}(\phi^n_{ij}+\phi^n_{i,j-1})}{2h}.$$

These complete the one time step.

https://doi.org/10.4208/cicp.301110.040811a Published online by Cambridge University Press

3.2 Cahn-Hilliard solver

In [73], authors analyzed a semi-discrete Fourier-spectral method for the numerical approximation of a phase-field model for the mixture of two incompressible fluids and implemented a semi-implicit scheme for the time discretization. An efficient moving mesh spectral method for the phase-field model of two-phase flows with non-periodic boundary conditions was developed in [86]. Nonlinear multigrid methods have been developed to solve implicit discretizations of the Cahn-Hilliard equation [58]. In [41], authors introduced provably unconditionally stable mixed variational methods for phase-field models.

In [22], authors presented an efficient numerical methodology for the 3D computation of incompressible multi-phase flows described by conservative phase-field models. The numerical method employs adaptive mesh refinements (AMR) in concert with an efficient semi-implicit time discretization strategy and a linear, multi-level multigrid to relax high order stability constraints and to capture the flow's disparate scales at optimal cost. Only five linear solvers are needed per time-step. Their formulation is based on a mixed finite element method for space discretization and a new second-order accurate time integration algorithm. The fully-discrete formulation inherits the main characteristics of conserved phase dynamics, namely, mass conservation and nonlinear stability with respect to the free energy. They also proposed an adaptive time-stepping version of the new time integration method.

In [87], several efficient and energy stable time discretization schemes for the coupled nonlinear Cahn-Hilliard phase-field system for both the matched density case and the variable density case were constructed and were shown to satisfy discrete energy laws which are analogous to the continuous energy laws. In [108], a convexity-splitting scheme to discretize in the temporal variable and a nonconforming finite element method to discretize in the spatial variable was used. And the scheme preserved the mass conservation and energy dissipation properties of the original problem. In [34], the least squares spectral element method was used to solve the Cahn-Hilliard equation.

We will present numerical methods in finite difference formats [36, 62]. For finite element methods for the CH equation, refer to references [7,8,11,31]. We shall first discretize the CH equations (2.10c) and (2.10d), without the advection term in a two dimensional space, i.e., $\Omega=(a,b)\times(c,d)$. Three-dimensional discretization is analogously defined. Let ϕ_{ij} and μ_{ij} be approximations of $\phi(x_i,y_j)$ and $\mu(x_i,y_j)$. We first implement the zero Neumann boundary condition (2.3) by requiring that

$$\phi_{0j}=\phi_{1j},\quad \phi_{N_x+1,j}=\phi_{N_x,j},\quad \phi_{i0}=\phi_{i1}\quad\text{and}\quad \phi_{i,N_y+1}=\phi_{i,N_y}.$$

We define the discrete Laplacian by $\Delta_d\phi_{ij}=(\phi_{i-1,j}+\phi_{i+1,j}-4\phi_{ij}+\phi_{i,j-1}+\phi_{i,j+1})/h^2$ and we also define discrete energy as

$$\mathcal{E}^h(\boldsymbol{\phi}^n)=h^2\sum_{i=1}^{N_x}\sum_{j=1}^{N_y}\left(F(\phi_{ij}^n)+\frac{\epsilon^2}{2}[(\phi_{i+1,j}^n-\phi_{ij}^n)^2+(\phi_{i,j+1}^n-\phi_{ij}^n)^2]\right).$$

https://doi.org/10.4208/cicp.301110.040811a Published online by Cambridge University Press

3.2.1 A backward implicit scheme

Backward implicit scheme was used in [25]

$$\frac{\phi_{ij}^{n+1}-\phi_{ij}^{n}}{\Delta t}=\Delta_d(F'(\phi_{ij}^{n+1})-\epsilon^2\Delta_d\phi_{ij}^{n+1}).$$

3.2.2 The Crank-Nicolson scheme

A conservative nonlinear multigrid method for the Cahn-Hilliard equation with a variable mobility was proposed in [58]. The method uses the standard finite difference approximation in spatial discretization and the Crank-Nicolson scheme in temporal discretization:

$$\begin{aligned}&\frac{c_{ij}^{n+1}-c_{ij}^{n}}{\Delta t}=\nabla_d\cdot[M(c)_{ij}^{n+\frac{1}{2}}\nabla_d\mu_{ij}^{n+\frac{1}{2}}],\\&\mu_{ij}^{n+\frac{1}{2}}=\frac{1}{2}(F'(c_{ij}^{n+1})+F'(c_{ij}^{n}))-\frac{\epsilon^2}{2}\Delta_d(c_{ij}^{n+1}+c_{ij}^{n}).\end{aligned}$$

Discrete versions of mass conservation and energy dissipation was proved.

3.2.3 Unconditionally gradient stable scheme

Ideally, one would like a stable integration algorithm, which would allow accuracy requirements rather than stability limitations to determine the integration step size [100]. For dissipative dynamics such as the CH equations, a discrete time stepping algorithm is defined to be *gradient stable* only if the free energy is nonincreasing,

$$\mathcal{E}^h(\boldsymbol{\phi}^{n+1})\leq\mathcal{E}^h(\boldsymbol{\phi}^{n})\ \text{ for all } n. \tag{3.6}$$

Unconditionally gradient stability means that the conditions for gradient stability hold for *any* size of time step Δt [100]. Eyre [32,33] proved that if $\boldsymbol{\phi}^{n+1}$ is the solution of Eqs. (3.8c) and (3.8d) with a given $\boldsymbol{\phi}^{n}$, then the inequality (3.6) holds. Furihata et al. [37] have examined the boundedness of the solution of a finite difference scheme [28] using a discretized Lyapunov functional. Furihata [36] has shown that the decrease of the total energy implies boundedness of the discretized Sobolev norm of the solution, independent Δt and Δx.

We can show the pointwise boundedness of the numerical solution using the decrease of the discrete total energy functional. The following proof is independent of space dimensions, therefore, for simplicity of indexing, we present it in one dimensional space. Let $\boldsymbol{\phi}^{n}$ be a numerical solution satisfying the condition (3.6) for a discrete CH equation, then there exists a constant K for all n such that

$$\|\boldsymbol{\phi}^{n}\|_\infty\leq K. \tag{3.7}$$

https://doi.org/10.4208/cicp.301110.040811a Published online by Cambridge University Press

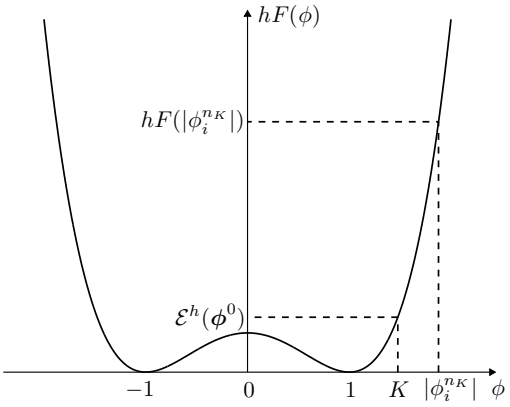

Figure 12: Graph of $hF(\phi)$.

We prove Eq. (3.7) by a contradiction. Assume on the contrary that there is an integer n_K, dependent on K, such that $\|\boldsymbol{\phi}^{n_K}\|_\infty > K$ for all K. Then there is an index i $(1 \le i \le N)$ such that $|\phi_i^{n_K}| > K$. Let K be the largest solution of $\mathcal{E}^h(\boldsymbol{\phi}^0) = hF(K)$, i.e.,

$$K = \sqrt{1+2\sqrt{\mathcal{E}^h(\boldsymbol{\phi}^0)/h}}.$$

Note that $K \ge 1$. Then, $F(\phi)$ is a strictly increasing function on (K,∞) (see Fig. 12) and the total energy is decreasing, so we have

$$\mathcal{E}^h(\boldsymbol{\phi}^0) = hF(K) < hF(|\phi_i^{n_K}|) \le \mathcal{E}^h(\boldsymbol{\phi}^{n_K}) \le \mathcal{E}^h(\boldsymbol{\phi}^0).$$

This contradiction implies that Eq. (3.7) should be satisfied.

Another compact alternative proof is as follows: for any i $(1 \le i \le N)$, it holds that $hF(\phi_i^n) \le \mathcal{E}^h(\boldsymbol{\phi}^n) \le \mathcal{E}^h(\boldsymbol{\phi}^0)$. The boundedness of ϕ_i^n follows from the profile of $hF(\phi)$.

3.2.4 Non-linearly stabilized splitting scheme

$$\frac{c_{ij}^{n+1}-c_{ij}^n}{\Delta t} = \Delta_d \nu_{ij}^{n+1} - \frac{1}{4}\Delta_d c_{ij}^n, \tag{3.8a}$$

$$\nu_{ij}^{n+1} = F'(c_{ij}^{n+1}) + \frac{1}{4}c_{ij}^{n+1} - \epsilon^2 \Delta_d c_{ij}^{n+1}, \tag{3.8b}$$

$$\frac{\phi_{ij}^{n+1}-\phi_{ij}^n}{\Delta t} = \Delta_d \nu_{ij}^{n+1} - \Delta_d \phi_{ij}^n, \tag{3.8c}$$

$$\nu_{ij}^{n+1} = F'(\phi_{ij}^{n+1}) + \phi_{ij}^{n+1} - \epsilon^2 \Delta_d \phi_{ij}^{n+1}. \tag{3.8d}$$

Numerical solution for non-linearly stabilized splitting scheme using a multigrid method can be found in [61].

https://doi.org/10.4208/cicp.301110.040811a Published online by Cambridge University Press

3.2.5 Linearly stabilized splitting scheme

In this scheme, the nonlinear term F' is treated as a source term. Therefore, we solve a system of linear equations

$$\begin{aligned}
&\frac{c_{ij}^{n+1}-c_{ij}^{n}}{\Delta t}=\Delta_d \nu_{ij}^{n+1}+\Delta_d(F'(c_{ij}^{n})-0.5c_{ij}^{n}),\\
&\nu_{ij}^{n+1}=0.5c_{ij}^{n+1}-\epsilon^2\Delta_d c_{ij}^{n+1},\\
&\frac{\phi_{ij}^{n+1}-\phi_{ij}^{n}}{\Delta t}=\Delta_d \nu_{ij}^{n+1}+\Delta_d(F'(\phi_{ij}^{n})-2\phi_{ij}^{n}),\\
&\nu_{ij}^{n+1}=2\phi_{ij}^{n+1}-\epsilon^2\Delta_d \phi_{ij}^{n+1}.
\end{aligned}$$

We note that since Eyre's theorem provides, in principle, only a subset of the possible gradient stable steps, complementary approaches for determining stability are desirable. In [100], authors extended the von Neumann linear stability analysis [3, 83] to arbitrary time steps.

3.2.6 Adaptive mesh refinement

Many multiphase flow problems involve multiple length scales. In order to effectively resolve the flow features in such cases, we need to consider adaptive grid refinement [97]. In [15], a local adaptive refinement method (CHARMS) proposed by Krysl, Grinspun and Schroder was used. Authors in [86] developed a moving mesh spectral method for the phase-field model of two phase flows with non-periodic boundary conditions. The method is based on a variational moving mesh PDE for the phase function, coupled with efficient semi-implicit treatments for advancing the mesh function, the phase function and the velocity and pressure in a decoupled manner.

Another approach is adaptive mesh refinement, in which the computational mesh is locally refined in regions where greater accuracy is desired [75]. In Fig. 13, we show an example of the grid structure used in the adaptive mesh refinement (AMR) [2]. In the non-adaptive multigrid on uniform grids, we have used a hierarchy of global grids, Ω_0, Ω_1, $\cdots$, Ω_l. In the adaptive approach, we introduce a hierarchy of increasingly finer grids, Ω_{l+1}, …, Ω_{l+l^*}, restricted to smaller and smaller subdomains around the phase-field interfacial transition zone. That is, we consider a hierarchy of grids, Ω_0, Ω_1, $\cdots$, Ω_{l+0}, Ω_{l+1}, $\cdots$, Ω_{l+l^*}. We denote Ω_{l+0} as level zero, Ω_{l+1} as level one, and so on. In Fig. 13 we have $l^*=2$.

The grid is adapted dynamically based on the undivided gradient. First, we tag cells that contain the front, i.e., those in which the undivided gradient of the phase-field is greater than a critical value. Then, the tagged cells are grouped into rectangular patches by using a clustering algorithm as in [10]. These rectangular patches are refined to form the grids at the next level. The process is repeated until a specified maximum level is reached. Next, we describe a nonlinear full approximation storage (FAS) multigrid method to solve the nonlinear discrete system, Eqs. (3.8c) and (3.8d), at an implicit time

https://doi.org/10.4208/cicp.301110.040811a Published online by Cambridge University Press

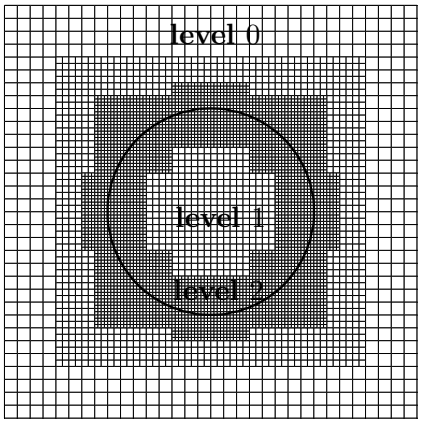

Figure 13: Block-structured local refinement. In this example, there are three levels.

level. See the [95] for additional details and background. The algorithm of the nonlinear multigrid method for solving the discrete system is as follows:

First, let us rewrite Eqs. (3.8c) and (3.8d) as

$$N(\phi^{n+1},\nu^{n+1})=(\varphi^n,\psi^n),$$

where $N(\phi^{n+1},\nu^{n+1}) = (\phi_{ij}^{n+1}/\Delta t-\Delta_d\nu_{ij}^{n+1},\nu_{ij}^{n+1}-(\phi_{ij}^{n+1})^3+\epsilon^2\Delta_d\phi_{ij}^{n+1})$ and the source term is $(\varphi^n,\ \psi^n)=(\phi_{ij}^n/\Delta t-\Delta_d\phi_{ij}^n,0)$. Using the above notations on all levels $k=0,1,\cdots,l,l+1,\cdots,l+l^*$, an adaptive multigrid cycle is formally written as follows: First we calculate φ_k^n, ψ_k^n on all levels and set the previous time solution as the initial guess, i.e., $(\phi_k^0,\nu_k^0)=(\phi_k^n,\nu_k^n)$

$$(\phi_k^{m+1},\nu_k^{m+1})=ADAPTIVEcycle(k,\phi_k^m,\phi_{k-1}^m,\nu_k^m,\nu_{k-1}^m,N_k,\varphi_k^n,\psi_k^n,\varsigma).$$

1) Presmoothing

- Compute $(\bar\phi_k^m,\ \bar\nu_k^m)$ by applying ς smoothing steps to $(\phi_k^m,\ \nu_k^m)$ on Ω_k

  $$(\bar\phi_k^m,\ \bar\nu_k^m)=SMOOTH^{\varsigma}(\phi_k^m,\nu_k^m,N_k,\varphi_k^n,\psi_k^n),$$

  where one $SMOOTH$ relaxation operator step consists of solving Eqs. (3.10a) and (3.10b) given below by 2×2 matrix inversion for each i and j. Rewriting Eqs. (3.8c) and (3.8d), we get

  $$\frac{\phi_{ij}^{n+1}}{\Delta t}+\frac{4}{h^2}\nu_{ij}^{n+1}=\varphi_{ij}^n+\frac{1}{h^2}(\nu_{i+1,j}^{n+1}+\nu_{i-1,j}^{n+1}+\nu_{i,j+1}^{n+1}+\nu_{i,j-1}^{n+1}), \tag{3.9a}$$

  $$-\frac{4\epsilon^2}{h^2}\phi_{ij}^{n+1}-(\phi_{ij}^{n+1})^3+\nu_{ij}^{n+1}=\psi_{ij}^n-\frac{\epsilon^2}{h^2}(\phi_{i+1,j}^{n+1}+\phi_{i-1,j}^{n+1}+\phi_{i,j+1}^{n+1}+\phi_{i,j-1}^{n+1}). \tag{3.9b}$$

- Next, we replace $\phi_{\alpha\beta}^{n+1}$ and $\nu_{\alpha\beta}^{n+1}$ in Eqs. (3.9a) and (3.9b) with $\bar\phi_{\alpha\beta}^m$ and $\bar\nu_{\alpha\beta}^m$ if $\alpha\le i$ and $\beta\le j$; otherwise we replace them with $\phi_{\alpha\beta}^m$ and $\nu_{\alpha\beta}^m$. Furthermore we linearize the nonlinear term

https://doi.org/10.4208/cicp.301110.040811a Published online by Cambridge University Press

$(\phi_{ij}^{n+1})^3$ as $(\bar{\phi}_{ij}^m)^3 \approx (\phi_{ij}^m)^3 + 3(\phi_{ij}^m)^2(\bar{\phi}_{ij}^m - \phi_{ij}^m)$. Then, the Gauss-Seidel relaxations are listed as the following equations:

$$\frac{\bar{\phi}_{ij}^m}{\Delta t} + \frac{4}{h^2}\bar{v}_{ij}^m = \varphi_{ij}^n + \frac{1}{h^2}(v_{i+1,j}^m + \bar{v}_{i-1,j}^m + v_{i,j+1}^m + \bar{v}_{i,j-1}^m), \tag{3.10a}$$

$$-\left(\frac{4\epsilon^2}{h^2} + 3(\phi_{ij}^m)^2\right)\bar{\phi}_{ij}^m + \bar{v}_{ij}^m = \psi_{ij}^n - 2(\phi_{ij}^m)^3 - \frac{\epsilon^2}{h^2}(\phi_{i+1,j}^m + \bar{\phi}_{i-1,j}^m + \phi_{i,j+1}^m + \bar{\phi}_{i,j-1}^m). \tag{3.10b}$$

2) *Coarse-grid correction*

- Compute

$$(\bar{\phi}_{k-1}^m, \bar{v}_{k-1}^m) = \begin{cases} I_k^{k-1}(\bar{\phi}_k^m, \bar{v}_k^m), & \text{on } \Omega_{k-1} \cap \Omega_k, \\ (\phi_{k-1}^m, v_{k-1}^m), & \text{on } \Omega_{k-1} \setminus \Omega_k. \end{cases}$$

- Compute the right-hand side

$$(\varphi_{k-1}^n, \psi_{k-1}^n) = \begin{cases} I_k^{k-1}\{(\varphi_k^n, \psi_k^n) - N_k(\bar{\phi}_k^m, \bar{v}_k^m)\} + N_{k-1} I_k^{k-1}(\bar{\phi}_k^m, \bar{v}_k^m), & \text{on } \Omega_{k-1} \cap \Omega_k, \\ (\varphi_{k-1}^n, \psi_{k-1}^n), & \text{on } \Omega_{k-1} \setminus \Omega_k. \end{cases}$$

- Compute an approximate solution $(\hat{\phi}_{k-1}^m, \hat{v}_{k-1}^m)$ of the coarse grid equation on Ω_{k-1}, i.e.,

$$N_{k-1}(\phi_{k-1}^m, v_{k-1}^m) = (\varphi_{k-1}^n, \psi_{k-1}^n). \tag{3.11}$$

If $k=1$, we explicitly invert a 2×2 matrix to obtain the solution. If $k>1$, we solve Eq. (3.11) by using $(\bar{\phi}_{k-1}^m, \bar{v}_{k-1}^m)$ as an initial approximation to perform an adaptive multigrid k-grid cycle:

$$(\hat{\phi}_{k-1}^m, \hat{v}_{k-1}^m) = \text{ADAPTIVEcycle}(k-1, \bar{\phi}_{k-1}^m, \phi_{k-2}^m, \bar{v}_{k-1}^m, v_{k-2}^m, N_{k-1}, \varphi_{k-1}^n, \psi_{k-1}^n, \varsigma).$$

- Compute the correction at $\Omega_{k-1} \cap \Omega_k$. $(\hat{u}_{k-1}^m, \hat{v}_{k-1}^m) = (\hat{\phi}_{k-1}^m, \hat{v}_{k-1}^m) - (\bar{\phi}_{k-1}^m, \bar{v}_{k-1}^m)$.
- Set the solution at the other points of $\Omega_{k-1} \setminus \Omega_k$. $(\phi_{k-1}^{m+1}, v_{k-1}^{m+1}) = (\hat{\phi}_{k-1}^m, \hat{v}_{k-1}^m)$.
- Interpolate the correction to Ω_k, $(\hat{u}_k^m, \hat{v}_k^m) = I_{k-1}^k(\hat{u}_{k-1}^m, \hat{v}_{k-1}^m)$.
- Compute the corrected approximation on Ω_k

$$(\phi_k^{m,\text{ after } CGC}, v_k^{m,\text{ after } CGC}) = (\bar{\phi}_k^m + \hat{u}_k^m, \bar{v}_k^m + \hat{v}_k^m).$$

3) Postsmoothing

$$(\phi_k^{m+1}, v_k^{m+1}) = SMOOTH^{\varsigma}(\phi_k^{m,\text{ after } CGC}, v_k^{m,\text{ after } CGC}, N_k, \varphi_k^n, \psi_k^n).$$

This completes the description of a nonlinear ADAPTIVE cycle. Please refer to [61, 101] for more details about the adaptive mesh refinement of the CH equation.

https://doi.org/10.4208/cicp.301110.040811a Published online by Cambridge University Press

4 Numerical applications

Phase-field models were applied to many applications and some of them are listed below.

4.1 Non-Newtonian flow

A diffuse-interface model was applied to drop coalescence and retraction involving Newtonian and non-Newtonian Oldroyd-*B* fluids [106]. Drop dynamics plays a central role in defining the interfacial morphology in two-phase complex fluids such as emulsions and polymer blends. To model and simulate drop behavior in such systems, one has to deal with the dual complexity of non-Newtonian rheology and evolving interfaces. Authors used a two-dimensional implementation of the method to simulate drop coalescence after head-on collision and drop retraction from an elongated initial shape in a quiescent matrix. One of the two phases is a viscoelastic fluid modeled by an Oldroyd-*B* equation and the other is Newtonian. Numerical results show that after drop collision, film drainage is enhanced when either phase is viscoelastic and drop coalescence happens more readily than in a comparable Newtonian system. The last stage of coalescence is dominated by a short-range molecular force in the model that is comparable to van der Waals force. The retraction of drops from an initial state of zero-velocity and zero-stress is hastened at first, but later resisted by viscoelasticity in either component. When retracting from an initial state with pre-existing stress, produced by cessation of steady shearing, viscoelasticity in the matrix hinders retraction from the beginning while that in the drop initially enhances retraction but later resists it. These results and the physical mechanisms were consistent with prior experimental observations. For more details about these non-Newtonian flows, please refer to [106].

4.2 Microtube flow

The phase-field method was applied to the simulations of air-water two-phase bubbly and slug flows in a $600\mu m$ microtube [46]. Accurate calculation of surface tension force is critically important for numerical simulation of gas-liquid two-phase flows at small capillary number. The surface tension force is represented by a chemical potential gradient. The numerical results show that the chemical potential formulation of surface tension force can reduce the magnitude of parasitic flow to the level of truncation error. This is because exchange between kinetic and surface energy is appropriately calculated. The method is applied to the simulations of air-water two-phase bubbly and slug flows in a microtube of $600\mu m$. The Reynolds numbers are 60-200, and the capillary number is $\mathcal{O}(10^{-3})$. The simulated gas bubble shape and two-phase flow patterns are in good agreement with experimental results. The pressure drop, represented by Lockhart-Martinelli correlation, is found larger than that proposed for tubes in millimeter.

https://doi.org/10.4208/cicp.301110.040811a Published online by Cambridge University Press

4.3 Droplet impact on a solid surface

The impact of micron-size drops on a smooth, flat, chemically homogeneous solid surface was studied using a diffuse-interface model. The model is based on the Cahn-Hilliard theory that couples thermodynamics with hydrodynamics, and is extended to include non-90° contact angles. The influence of various process and material parameters such as impact velocity, droplet diameter, viscosity, surface tension and wettability on the impact behavior of drops was investigated. The wettability significantly affects the impact behavior and this is particularly demonstrated with an impact at $Re=130$ and $We=1.5$, where for $\theta<60$ the droplet oscillates a few times before attaining equilibrium while for $\theta\geq 60$ partial rebound of the droplet occurs, i.e., the droplet breaks into two unequal sized drops. The size of the part that remains in contact with the solid surface progressively decreases with increasing θ until at a value $\theta\approx 120^\circ$ a transition to total rebound happens. When the droplet rebounds totally, it has a top-heavy shape [54].

4.4 Spinodal decomposition under gravity and shear flow

Authors in [5] used a phase-field model to compute the phase ordering kinetics coupled with fluid dynamics in order to study the effect of gravity and shear on critical spinodal decomposition of a binary mixture. When a system such as a binary liquid is cooled rapidly from a homogeneous phase into a two-phase region, domains of the two equilibrium phases form and grow (coarsen) with time. In the absence of external forcing, such as by gravity or an imposed shear flow, a dynamical-scaling regime emerges in which the domain morphology is statistically self-similar at different times, with an overall length-scale (coarsening scale) that grows with time. In the paper, the scaling phenomenology was reviewed, the time-dependence of the coarsening scale was discussed, and the influence of external drives such as gravity and shear flow was addressed. In particular, they found that multiple length scales emerge since in the shear case the system coarsens more rapidly in the mean flow direction while in the gravity case the coarsening is more rapid in the direction of the gravity. Further for the shear they showed that it is possible to control the asymptotic morphology of the phase separation in order to obtain either lamellae or cylindrical structures and potentially create for example nano-conductive wires or materials with particular optical properties. Investigating gravitational effects they found that scaling laws are significantly affected even for low gravity.

4.5 Stability of a lamellar domain under an external flow

The stability of a lamellar domain in phase-separating binary fluids under an external flow was investigated in [66]. Authors take into account effects of diffusion and surface tension at an interface using the Navier-Stokes and the Cahn-Hilliard equations. Stability eigenvalues are evaluated for various values of the Peclet number, the spacing between the interfaces, and the Reynolds number. It was found that the lamellar domain becomes unstable at a finite wavenumber before the flow when the Reynolds number increases.

https://doi.org/10.4208/cicp.301110.040811a Published online by Cambridge University Press

The instability of the interface occurs on conditions that the interface is situated near a wall or the Peclet number is large. The instability stems from the interaction between disturbances of the flow and the diffusive interface.

4.6 Marangoni convection

Using the phase-field model, authors in [12] have analyzed the problem of the Marangoni convection in a liquid-gas system with a deformable interface, heated from below. In order to describe both Marangoni instabilities with short and long wavelengths, an additional force component must be considered in the Navier-Stokes equation. This term describes the coupling of the temperature to the velocity field via the phase-field function. It results by minimizing the free-energy functional of the system. For a bidimensional problem in linear approximation they performed a numerical code that successfully computes both Marangoni instabilities. In the limit of sharp and rigid interfaces, their results are compared with the literature.

5 Computational experiments

In this section, we present numerical experiments to test the capabilities of the phase-field models for multi-component fluid flows. The experiments are the phase separation, effect of the Peclet number, long time evolution of the Rayleigh-Taylor instability, the Rayleigh-instability, liquid-liquid jet pinchoff, contact angle problem for a binary mixture. Also, another set of experiments for the ternary and the quaternary mixtures are an equilibrium contact angle of a three components system and surface tension driven drop coalescence, respectively.

5.1 A binary fluid

5.1.1 The relation between the ϵ value and the width of the transition layer

In our first numerical experiment, we consider the relation between the ϵ value and the width of the transition layer for the CH Eqs. (2.2a) and (2.2b) without the advection term $\mathbf{u}\cdot\nabla\phi$. For the numerical solution we apply the non-linearly stabilized splitting scheme (3.8c) and (3.8d). From our choice of the equilibrium profile $\phi(x)=\tanh(x/(\sqrt{2}\epsilon))$ on an infinite domain, the concentration field varies from -0.9 to 0.9 over a distance of about $\xi=2\sqrt{2}\epsilon\tanh^{-1}(0.9)$ (see Fig. 14). Therefore, if we want this value to be about m grid points, then $\epsilon_m=hm/[2\sqrt{2}\tanh^{-1}(0.9)]$, where h is the grid size. In most cases, we use $4\le m\le 8$. If m is too small, then it is difficult to calculate higher order derivatives of the phase-field because the interface transition profile is so abrupt. On the other hand, if you too large value of m, then the interface profile is too diffused. To confirm this formula, we ran a simulation with the initial condition $\phi(x,y,0)=0.01\text{rand}(x,y)$ on the domain $\Omega=[0,64]\times[0,64]$ with $h=1$, $\Delta t=0.05\times 64^2$, and ϵ_4. Here, $\text{rand}(x,y)$ is a random number

https://doi.org/10.4208/cicp.301110.040811a Published online by Cambridge University Press

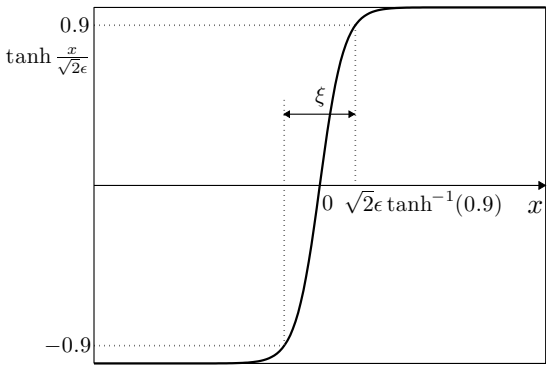

Figure 14: The concentration field varies from -0.9 to 0.9 over a distance of about $\xi = 2\sqrt{2}\epsilon\tanh^{-1}(0.9)$.

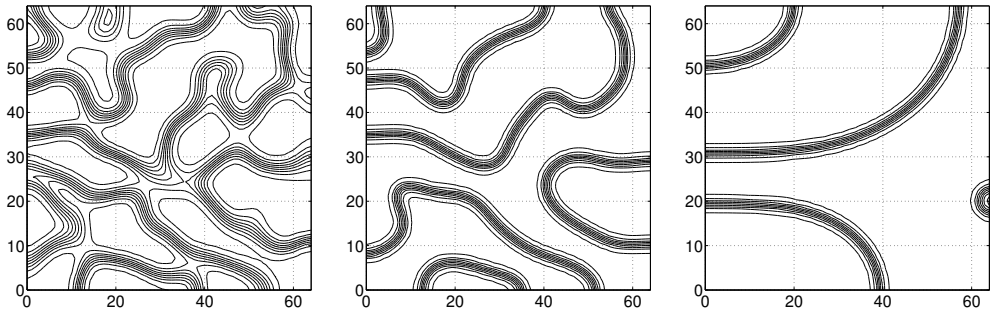

(a) $t = 25\Delta t$ (b) $t = 50\Delta t$ (c) $t = 500\Delta t$

Figure 15: The evolution of an initial random concentration, $\phi(x,y,0) = 0.01\text{rand}(x,y)$. The times are shown below each figure.

between -1 and 1. In Fig. 15, we see that the transition layer (from $\phi = -0.9$ to $\phi = 0.9$) is about 4 grid points at time $t = 102400$.

From our choice of the homogeneous free energy density and the equilibrium profile $c(x) = 0.5(1-\tanh(x/(2\sqrt{2}\epsilon)))$, the concentration field varies from 0.05 to 0.95 over a distance of about $4\sqrt{2}\epsilon\tanh^{-1}(0.9)$. That is $\epsilon_m = hm/[4\sqrt{2}\tanh^{-1}(0.9)]$.

5.1.2 Adaptive mesh refinement

The system of equations we solve are the CH Eqs. (2.2a) and (2.2b) without the advection term $\mathbf{u}\cdot\nabla\phi$. For the numerical solution we apply the non-linearly stabilized splitting scheme (3.8c) and (3.8d) with the adaptive mesh refinement technique. The initial state is taken to be $\phi(x,y,0) = -0.4 + 0.05\text{rand(x,y)}$ on the computational domain $\Omega = [0,1]\times[0,1]$. We use the simulation parameters $\epsilon = 0.005$ and $\Delta t = 1/256$. We also use a base 64×64 mesh with two levels of refinement. Therefore, the effective fine mesh size is 256×256. Fig. 16 shows an evolution of the mesh and the $\phi(x,y,t) = 0$ contours under spinodal decomposition at times $t = 2.34$, 7.42, and 39.06. Please refer to [61, 101] for more details about the adaptive mesh refinement of the CH equation.

https://doi.org/10.4208/cicp.301110.040811a Published online by Cambridge University Press

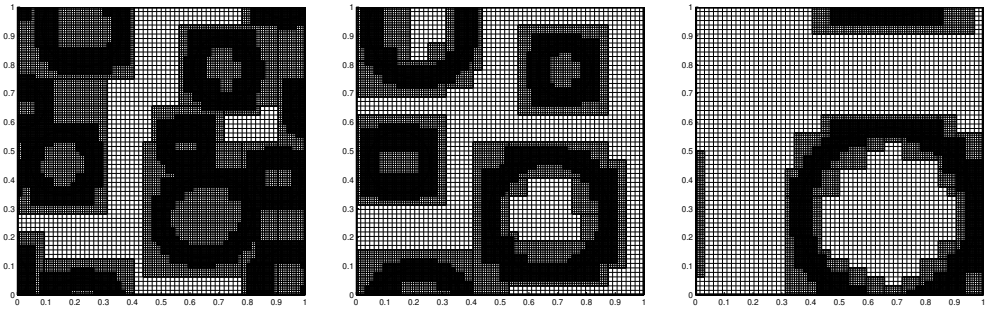

(a) $t=2.34$ (b) $t=7.42$ (c) $t=39.06$

Figure 16: Evolution of the mesh and the $\phi(x,y,t)=0$ contours under spinodal decomposition with an average concentration $c_{average}=-0.4$. The times are shown below each figure. The effective fine grid resolution for 2 levels of adaptivity is 256×256.

5.1.3 Effect of the Peclet number

The Rayleigh-Taylor instability would occur for any perturbation along the interface between a heavy fluid on top of a lighter fluid and is characterized by the density ratio between the two fluids. The density difference is represented by the Atwood number $At=(\rho_2-\rho_1)/(\rho_2+\rho_1)$, where ρ_1 and ρ_2 are the densities of the lighter and heavier fluid, respectively. In this section, we investigate the effect of the Peclet number, demonstrate convergence of our scheme numerically, and simulate the Rayleigh-Taylor instability for a long time. Unless otherwise specified, we take the initial state as

$$\phi(x,y,0)=\tanh\left(\frac{y-2-0.1\cos(2\pi x)}{\sqrt{2}\epsilon}\right) \tag{5.1}$$

on the computational domain $\Omega=[0,1]\times[0,4]$, which represents a planar interface superimposed by a perturbation of wave number $k=1$ with an amplitude of 0.1. The density ratio is $\rho_2:\rho_1=3:1$, i.e., $At=0.5$. We use the simulation parameters such as the uniform time step, $\Delta t=0.00125\sqrt{2}$, $\epsilon=0.01$, $Re=3000$, and $Fr=1$.

In order to investigate the effect of the Peclet number, we consider the evolution of the interface with different Peclet numbers. The system of equations we solve are Eqs. (2.30a)-(2.30d) without the surface term. We apply the boundary condition (3.5). The initial state is given in Eq. (5.1) and the zero-level set is shown in Fig. 17(a). In this test, the number of grid points is 128×512. Fig. 17(b), (c), and (d) represent evolutions of the interface with Peclet numbers $Pe=0.01/\epsilon$, $1/\epsilon$, and $100/\epsilon$, respectively. In the case of $Pe=0.01/\epsilon$, the evolution of the interface did not fully occur (we can not see the rolling-up of the falling fluid). And in the case of $Pe=100/\epsilon$, the contour line is not uniform. Therefore, the appropriate Peclet number is $Pe=1/\epsilon$. It is clear that the interface evolution is significantly affected by Pe numbers. Larger Pe numbers result in non-smooth concentration profiles, while smaller Pe numbers result in too much diffusion. We note that the optimal Peclet number is dependent on flow problems because the number is defined as $Pe=U_cL_c/(M\mu_c)$.

https://doi.org/10.4208/cicp.301110.040811a Published online by Cambridge University Press

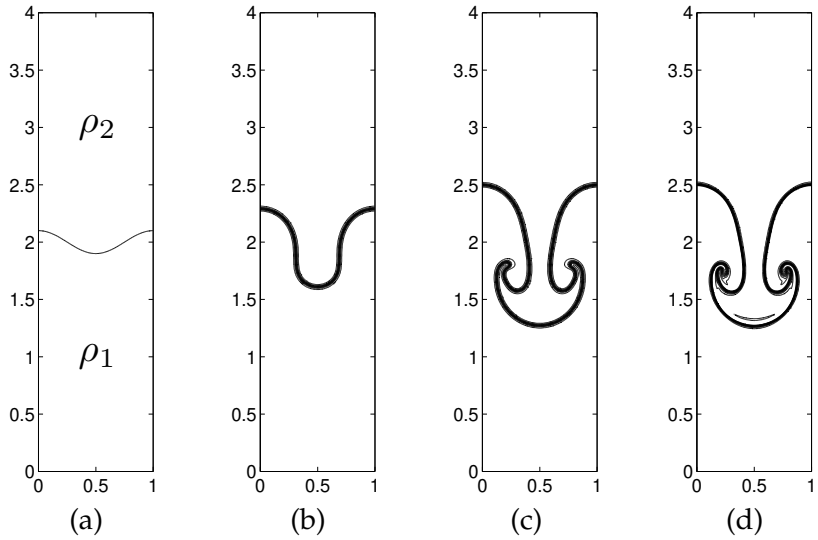

Figure 17: (a) The zero-level set of the initial profile, $\phi(x,y,0)=\tanh(\frac{y-2-0.1\cos(2\pi x)}{\sqrt{2}\epsilon})$. The effect of the Peclet number on the temporal evolution of the interface at dimensionless time $t=1.75$: (b) $Pe=0.01/\epsilon$, (c) $Pe=1/\epsilon$, and (d) $Pe=100/\epsilon$. Contour levels are -0.9, -0.7, $\cdots$, 0.7, 0.9.

5.1.4 Long time evolution of the Rayleigh-Taylor instability

Next we show the long time evolution of the classical Rayleigh-Taylor instability with a phase-field method. Despite of the long history of numerical simulations for the Rayleigh-Taylor instability, almost all results were relatively short time experiments. This is partly because of the way of treating the pressure boundary conditions. With a time-dependent pressure boundary condition (3.5) through a time-dependent density field at the boundary, we can perform long time evolutions resulting in an equilibrium state.

The initial state is given in Eq. (5.1) and the number of grid points is 128×512. The system of equations we solve and parameters are same as before. The evolution of the interface is shown in Fig. 18 at $t=0$, 1, 1.5, 1.75, 2, 2.25, 2.5, 6, 8, 12, 18, 24, 30, and 50. The rolling-up of the falling fluid can be clearly seen. At time $t=50$, the heavier fluid has fallen down completely. Please refer to [68] for more details about long time evolution of the Rayleigh-Taylor instability and numerical solutions.

5.1.5 Rayleigh instability

In this section we apply the phase-field method to Rayleigh's capillary instability problems in which surface tension effects and topological changes are present. We will consider a long cylindrical thread of a viscous fluid 1, the viscosity and density of which are denoted by η_i and ρ_i respectively, in an infinite mass of another viscous fluid 2 of viscosity η_o and ρ_o. In the unperturbed state, the interface has a perfectly cylindrical shape with a circular cross-section of radius a.

https://doi.org/10.4208/cicp.301110.040811a Published online by Cambridge University Press

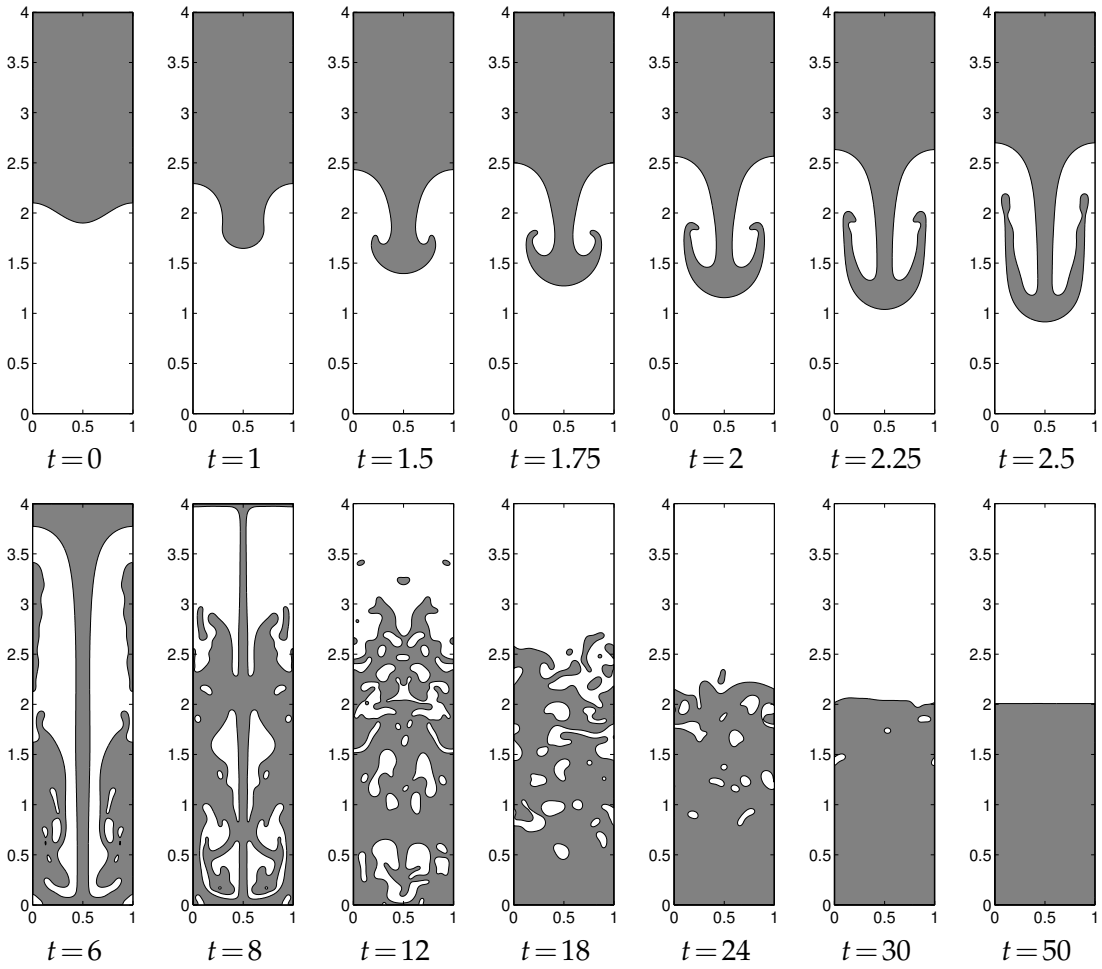

Figure 18: Long time evolution of the Rayleigh-Taylor instability simulation with $At = 0.5$. The dimensionless times are shown below each figure.

In this analysis, the growth of an initially cosinusoidal perturbation to the thread radius a, at the leading order, is observed to be given by

$$R(z,t) = a + \alpha(t)\cos(kz)$$

and $\alpha(t) = \alpha_0 e^{int}$, where in is the growth rate and α_0 is the amplitude of the initial perturbation. In Fig. 19, these parameters are shown schematically. The domain is axisymmetric and the bottom boundary is the axis of symmetry. Since we consider axisymmetric flows, therefore there is no flow in the θ (azumusal) direction and all θ derivatives are identically zero. So we consider only two variables, r the radial direction and z the axial direction. We define the fluid velocity by the vector $\mathbf{u} = (u,w)$, where $u = u(r,z)$ is the radial component of velocity and $w = w(r,z)$ is the component in the axial direction. The governing

https://doi.org/10.4208/cicp.301110.040811a Published online by Cambridge University Press

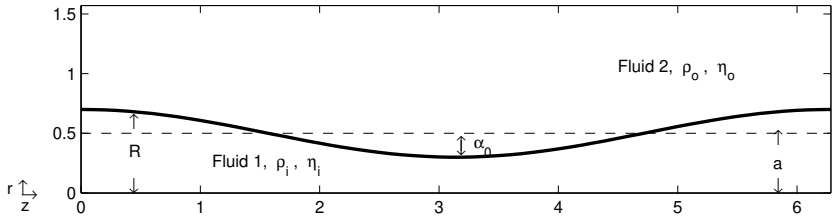

Figure 19: Schematic of a cylindrical thread of viscous fluid 1 embedded in another viscous fluid 2.

equations for axisymmetric flow without the gravitational force are

$$\frac{1}{r}(ru)_r+w_z=0, \tag{5.2a}$$

$$u_t+uu_r+wu_z=-p_r+\frac{1}{Re}\left[\frac{1}{r}(r(2\eta u_r))_r+(\eta(w_r+u_z))_z-\frac{2\eta u}{r^2}\right]+F_1, \tag{5.2b}$$

$$w_t+uw_r+ww_z=-p_z+\frac{1}{Re}\left[\frac{1}{r}(r\eta(w_r+u_z))_r+(2\eta w_z)_z\right]+F_2, \tag{5.2c}$$

$$c_t+uc_r+wc_z=\frac{1}{Pe}\left[\frac{1}{r}(rM(c)\mu_r)_r+(M(c)\mu_z)_z\right], \tag{5.2d}$$

$$\mu=f(c)-\epsilon^2\left[\frac{1}{r}(rc_r)_r+c_{zz}\right], \tag{5.2e}$$

where

$$(F_1,F_2)=\frac{\epsilon\alpha}{We}\nabla\cdot(|\nabla c|^2I-\nabla c\otimes\nabla c),\quad \nabla c=(c_r,c_z),\quad \nabla\cdot(\phi,\psi)=\frac{1}{r}(r\phi)_r+\psi_z,$$

where the indexes t, r and z refer to differentiation with respect to the variable. In this computation we use the following parameters: a=0.5, $\alpha(0)$=0.05, k=1, ϵ=0.02, Re=0.16, $We=0.016$, $Pe=100/\epsilon$, mesh size $h=2\pi/256$ and viscosity ratio $\beta=0.5$. The initial concentration field and velocity fields are given by

$$c(r,z,0)=0.5\left[1-\tanh\left(\frac{r-0.5-0.05\cos(z)}{2\sqrt{2}\epsilon}\right)\right],$$
$$u(r,z,0)=w(r,z,0)=0$$

on a domain, $\Omega=\{(r,z)|0\le r\le 2\pi \text{ and } 0\le z\le 2\pi\}$. In the thread evolution, the deformation growth rates are consistent with the predictions of the linear stability analysis (e.g., see Tomotika [94]).

An example of the long time evolution of the interface profile is shown in Fig. 22. In the early states ($t=0.1$ and 1.5) the surface contour has only one minimum at exactly $z=\pi$. As the time increases, nonlinearities become important and the initially cosinusoidal shape of the interface changes to a more complex form. The zone of the minimum moves symmetrically off the center ($z=\pi$), giving rise to satellite drops. These satellite drop formations could be attributed to the nonlinear terms in the equations of motion [23]. Please refer to [57] for more details about the axisymmetric Rayleigh instability and numerical solutions.

https://doi.org/10.4208/cicp.301110.040811a Published online by Cambridge University Press

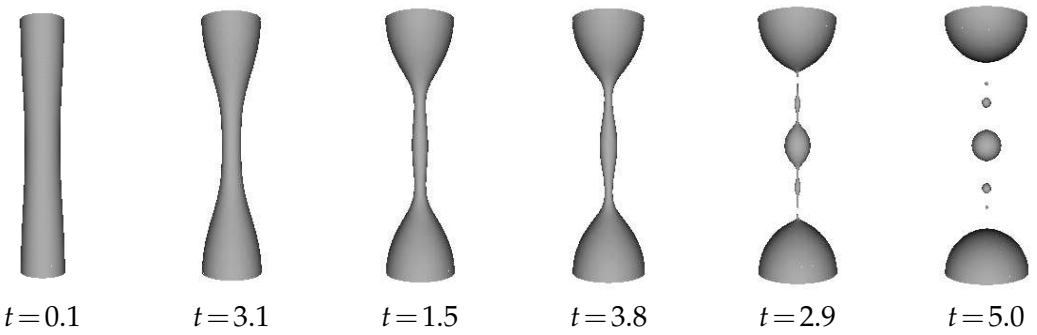

Figure 20: Time evolution leading to multiple pinch-offs. The viscosity ratio is 0.5, $\epsilon=0.02$, $Pe=100/\epsilon$, $Re=0.16$ and $We=0.016$. The dimensionless times are shown below each figure.

5.1.6 Liquid-liquid jet

Next, we consider a liquid-liquid jet that pinches off, resulting in droplets. The experimental setup, consisting of a tank, a pump, a needle valve, a flowmeter, and a forcer, is illustrated in Fig. 21(a). The dimensions of the tank are $20.3\times20.3\times56cm^3$. A magnetic-driven pump generates a steady flow controlled by a needle valve. The flow (a water/glycerin mixture) passes through a honeycomb straightener before exiting a nozzle into an ambient layer of the Dow Corning fluid. More details about the experimental setup are given in [76].

The flow configuration that was investigated numerically in our study is shown in Fig. 21(b). The jet of a viscous fluid, fluid 1, is injected vertically from a circular noz-

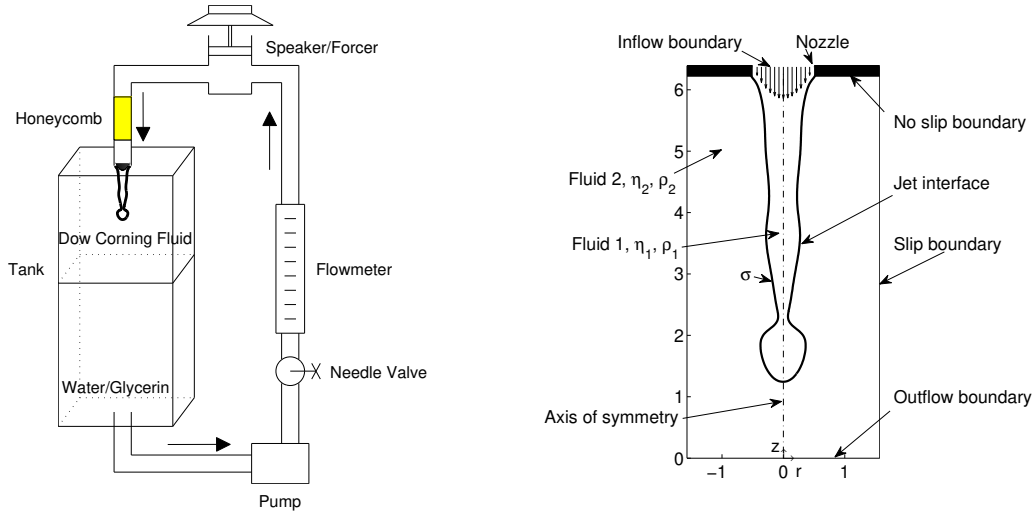

Figure 21: (a) Recirculating jet facility. (b) Liquid/liquid jet flow configuration.

https://doi.org/10.4208/cicp.301110.040811a Published online by Cambridge University Press

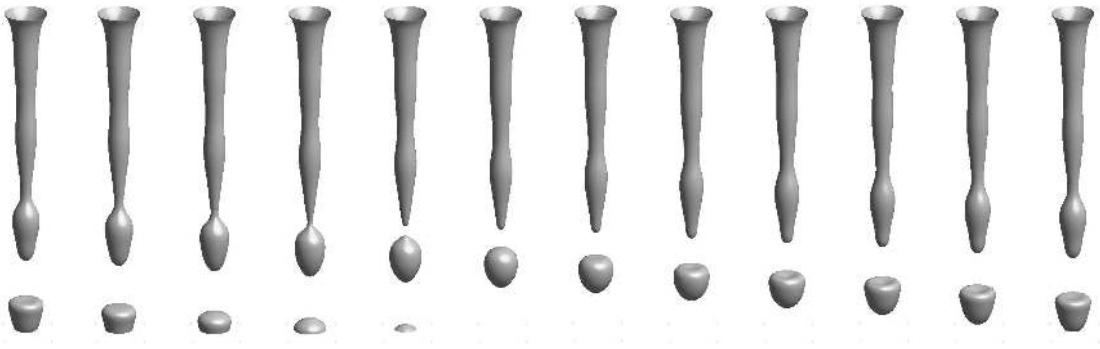

Figure 22: The phase-locked sequence for jet pinchoff.

zle downwards into a tank of a stationary mutually saturated immiscible fluid, fluid 2. The viscosity and density of the inner jet (fluid 1) are denoted by η_1 and ρ_1, respectively. Likewise, those of the outer ambient fluid (fluid 2) are denoted by η_2 and ρ_2, respectively. The domain is axisymmetric with the center line being the axis of symmetry. The system of governing equations are same to previous Eqs. (5.2a)-(5.2e) with the additional gravitational force term. The initial concentration field and velocity fields are given by

$$c(r,z,0)=0.5\Big[1-\tanh\Big(\frac{r-0.5-0.05\cos(z)}{2\sqrt{2}\epsilon}\Big)\Big],$$
$$u(r,z,0)=w(r,z,0)=0$$

on the domain $\Omega=\{(r,z)|0\le r\le 0.5\pi \text{ and } 0\le z\le 4\pi\}$. In this computation, we use the following parameters: $\epsilon=0.02$, $Re=58$, $We=0.016$, $St=3.5$, and $Pe=100/\epsilon$. Sequences of phase-locked images are shown in Fig. 22. As the liquid filament is stretched by gravity, a neck forms, elongates, and becomes thinner. In the meantime, the lower end of the filament turns into a round drop due to capillary forces. The falling drop continues to stretch the thread, and eventually the Rayleigh instability leads to a pinchoff of the main drop [105].

The normalized axial velocity (w) contours of the forced flow are shown in Fig. 23(a) and (b). The highest contour level is 0, and succeeding levels are reduced by 1. We can see that, before pinchoff, the maximum axial velocity is approximately located at the jet neck. The fluid is, thus, accelerating into the neck and acting to increase the volume of the drop. After the pinchoff, the maximum velocity still resides inside the drop. The normalized vorticity field (w_r-u_z) contours of the forced flow are shown in Fig. 23(c) and (d). Solid lines represent positive vorticity. The lowest contour level is 0.05. Succeeding levels are incremented by 0.5. Dotted lines represent negative vorticity. The highest contour level is -0.05. Succeeding levels are reduced by 0.5. Before pinchoff, two opposite signed vorticities develop around the jet neck and act to encourage pinchoff. A positive vorticity makes the fluid rotate clockwise while a negative vorticity makes the fluid rotate

https://doi.org/10.4208/cicp.301110.040811a Published online by Cambridge University Press

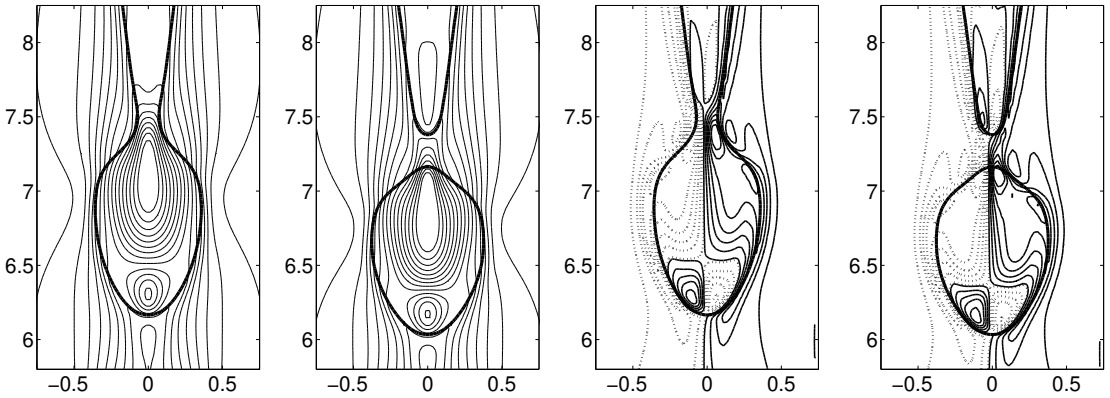

Figure 23: (a) and (b) are normalized axial velocity (w) contours of forced flow before and after pinchoff, respectively. The highest contour level is 0. Succeeding levels are reduced by 1. (c) and (d) are normalized vorticity field ($w_r - u_z$) contours of forced flow before and after pinchoff, respectively. The solid lines represent positive vorticity. The lowest contour level is 0.05. Succeeding levels are incremented by 0.5. The dotted lines represent negative vorticity. The highest contour level is -0.05. Succeeding levels are reduced by 0.5.

counterclockwise. After the drop pinches off, a small ring of inverted vorticity develops at the jet tip due to the recoiling interface there. These results are qualitatively in good agreement with the experimental data [76]. Please refer to [65] for more details about the pinchoff of liquid-liquid jets and numerical solutions.

5.1.7 Contact angle problem

Let us consider an equilibrium of an interface contacting a wall with a prescribed contact angle θ. The purpose of this section is to confirm contact angle boundary condition formula. The system of equations we solve are Eqs. (2.2a)-(2.2b) without the advection term. We apply the contact angle boundary condition (2.15a)-(2.15b). We take the simulation parameters, $h = 1/128$, $\epsilon = 0.13\sqrt{h}$, $\Delta t = 5/128$ and mesh size of 256×128 on the computational domain, $\Omega = [0,2] \times [0,1]$. The initial state is taken to be a rectangle, i.e.,

$$\phi(x,y,0) = \begin{cases} 1, & \text{if } 0.7 \le x \le 1.3 \text{ and } 0 \le y \le 0.4, \\ -1, & \text{otherwise.} \end{cases}$$

Fig. 24 shows evolutions of an interface with prescribed contact angle $\theta = 135^\circ$. The arrow shows the direction of the evolution and the thicker line corresponds to a steady shape. Please refer to [67] for more details about the contact angle problem and numerical solutions.

5.2 A ternary fluid

We now consider the situation of a ternary fluid consisting of three components. Following [88], we next investigated the spreading of a circular liquid lens (Fig. 25(a)) located at

https://doi.org/10.4208/cicp.301110.040811a Published online by Cambridge University Press

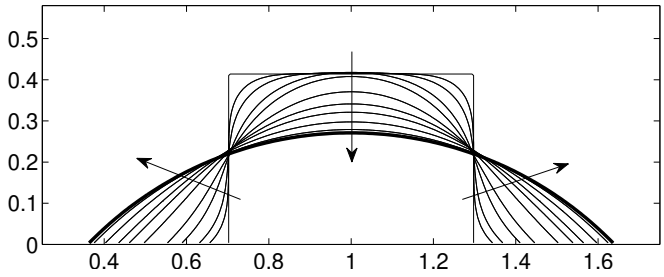

Figure 24: Evolutions of an interface with prescribed contact angle $\theta=135^\circ$. The arrow shows the direction of the evolution and the thicker line corresponds to a steady shape.

an interface between two other immiscible fluids. The system of equations we solve are Eqs. (2.19a)-(2.19f) without the gravitational force term. The initial condition is a circular droplet, Ω_2, (located at an interface between Ω_1 and Ω_3). The initial velocity was zero, i.e.,

$$c_1(x,y,0)=\max\left[0.5\left(1+\tanh\left(\frac{y-0.5}{2\sqrt{2}\epsilon}\right)\right)-c_2(x,y,0),0\right],$$
$$c_2(x,y,0)=0.5\left(1+\tanh\left(\frac{0.15-\sqrt{(x-0.5)^2+(y-0.5)^2}}{2\sqrt{2}\epsilon}\right)\right),$$
$$u(x,y,0)=v(x,y,0)=0.$$

The computational domain was $\Omega=[0,1]\times[0,1]$ and the mesh size was 256×256. The fluid viscosities were matched $(\eta_1=\eta_2=\eta_3)$, $Re=60$, $We_2=60$, and $We_1=We_3=36$. Please refer to [59] for more details about the definition of the non-dimensional parameters used here.

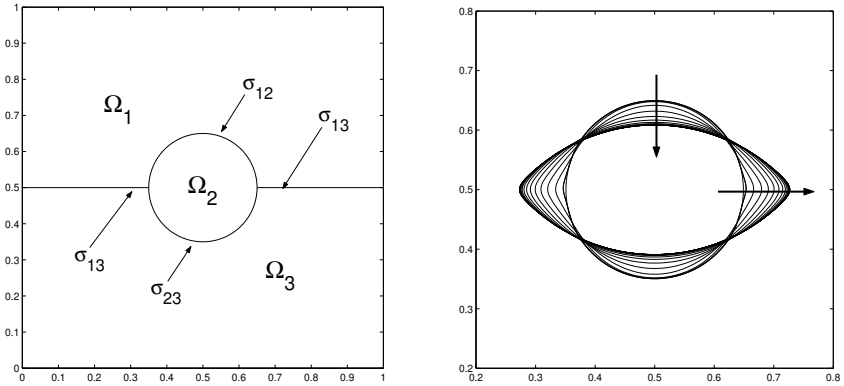

(a) (b)

Figure 25: (a) A schematic of the initial configuration: the upper fluid is in phase 1, the lower fluid is in phase 3, and the droplet is in phase 2. (b) The temporal evolution of the initial circular drop is shown for $We_2=60$ and $We_1=We_3=36$. The arrow shows the direction of the evolution. The most deformed line is the steady shape.

https://doi.org/10.4208/cicp.301110.040811a Published online by Cambridge University Press

In Fig. 25(b), the evolution of the $c_2 = 1/2$ contour line is shown. In this case, $\epsilon = 0.006/\sqrt{2}$, $Pe = 10/\epsilon$, $h = 1/256$, and $\Delta t = 0.05h$ were used. As the droplet spread, it reached an equilibrium shape. The most deformed curve was the numerical steady-state. Theoretically, the shape of the steady-state drop is controlled by the three surface tension coefficients. The equilibrium three-phase contact angle is determined by

$$\frac{\sin\theta_1}{\sigma_{23}} = \frac{\sin\theta_2}{\sigma_{13}} = \frac{\sin\theta_3}{\sigma_{12}}.$$

The relationship between the lens area A, its length d (the distance between two triple junctions), and the contact angles θ_i (see Fig. 8) of the i-th phase (Young's law) is

$$d = \Big(\frac{2(\pi-\theta_1)-\sin(2(\pi-\theta_1))}{8A\sin^2(\pi-\theta_1)} + \frac{2(\pi-\theta_3)-\sin(2(\pi-\theta_3))}{8A\sin^2(\pi-\theta_3)}\Big)^{-\frac{1}{2}}.$$

Thus, the accuracy of the steady lens shape can be measured by comparing the observed d with the analytical value. We found that there was very good agreement between the theoretical value, $d = 0.4596$ and the simulation result value, $d = 0.4539$. In [15], the numerical applications are performed with large ratio between densities and viscosities and three different surface tensions.

5.3 More than ternary fluid

We consider the dynamics of two droplets inside other elliptical drops embedded in the ambient liquid. The initial condition is that of two droplets, Ω_2 and Ω_3, enclosed by elliptical drops, Ω_1, which are also in the ambient fluid, Ω_4 (see Fig. 26). The initial velocity is zero, i.e.,

$$\begin{aligned}
c_1(x,y,0) &= 1-\frac{1}{2}\tanh\frac{\sqrt{5(x-1.28)^2+(y-2)^2}-1.5}{2\sqrt{2}\epsilon} - c_2(x,y,0)\\
&\quad -\frac{1}{2}\tanh\frac{\sqrt{5(x-2.72)^2+(y-2)^2}-1.5}{2\sqrt{2}\epsilon} - c_3(x,y,0),\\
c_2(x,y,0) &= \frac{1}{2}\Big(1-\tanh\frac{\sqrt{(x-1.28)^2+(y-2)^2}-r}{2\sqrt{2}\epsilon}\Big),\\
c_3(x,y,0) &= \frac{1}{2}\Big(1-\tanh\frac{\sqrt{(x-2.72)^2+(y-2)^2}-r}{2\sqrt{2}\epsilon}\Big),\\
u(x,y,0) &= v(x,y,0) = 0,
\end{aligned}$$

where $r = 0.4$ is the radius of the small drops.

We solved Eqs. (2.28a)-(2.28d) on the computational domain, $\Omega = [0,4]\times[0,4]$ with a uniform grid of 256×256, time step, $\Delta t = 0.05/256$, and $\epsilon = 0.015$. Periodic boundary conditions for both directions are applied. We take the viscosities of the components to

https://doi.org/10.4208/cicp.301110.040811a Published online by Cambridge University Press

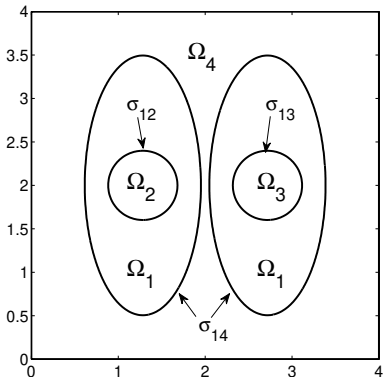

Figure 26: Schematic diagram of four-component fluid.

be matched as well as the following parameters. $We_{14}=We_{23}=We_{24}=We_{34}=5$, $We_{12}=10$, $We_{13}=20$, $Re=5$ and $Pe=1/\epsilon$.

We show in Fig. 27 the temporal evolution of the dynamics of two droplets inside other elliptical drops embedded in the ambient liquid. The driving force for the flow is surface tension. Fluid Ω_1 is represented by the gray region; fluid Ω_2 by the dark gray region; fluid Ω_3 by the black region; and fluid Ω_4 by the white region. Initially the elliptical drops deform to reduce the higher curvature, then, coalescence occurs around $t=3.91$. Eventually, at later times, all interfaces became circular equilibrium shapes (see Fig. 27(f)). Fig. 28 shows the pressure distribution at $y=2$. According to the Laplace

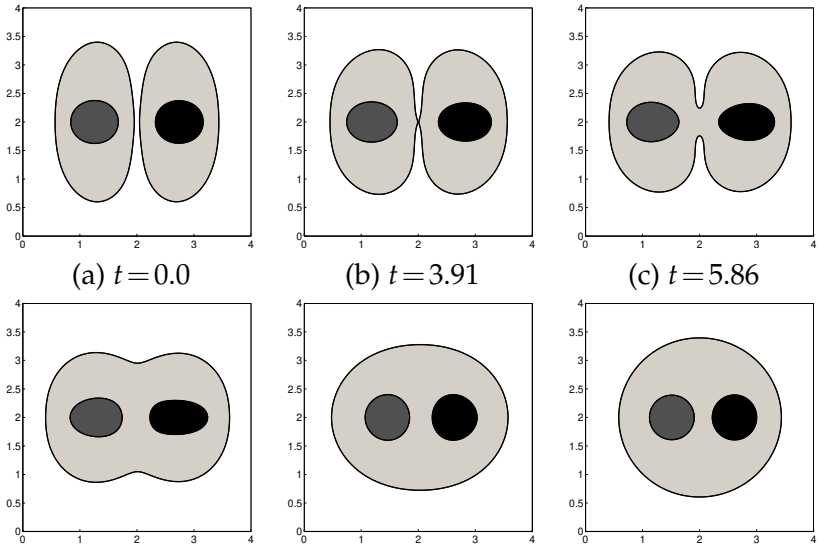

(a) $t=0.0$ (b) $t=3.91$ (c) $t=5.86$

(d) $t=9.77$ (e) $t=17.58$ (f) $t=97.66$

Figure 27: Temporal evolution. Fluid Ω_1 is represented by the gray region; fluid Ω_2 by the dark gray region; fluid Ω_3, by the black region; and fluid Ω_4, by the white region.

https://doi.org/10.4208/cicp.301110.040811a Published online by Cambridge University Press

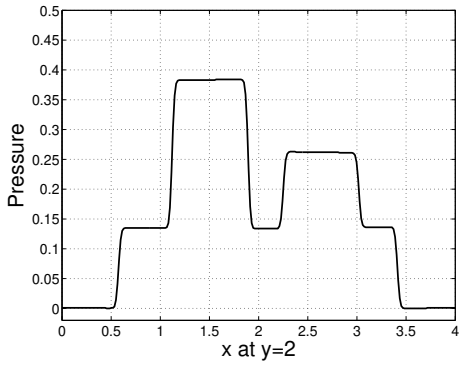

Figure 28: A slice plot of the pressure field on $y=2$.

formula, (2.12), the theoretical drop pressure jumps across the circles:

$$[p]_{\Gamma_{12}}=\frac{1}{rWe_{12}}=0.25, \qquad [p]_{\Gamma_{13}}=\frac{1}{rWe_{13}}=0.125 \quad \text{and} \quad [p]_{\Gamma_{14}}=\frac{1}{RWe_{14}}=0.1416,$$

where $R=1.4127$ is the measured radius of the largest circle in Fig. 27(f). The numerical values of the pressure jump across the drops are $[p]^{num}_{\Gamma_{12}}$=0.248, $[p]^{num}_{\Gamma_{13}}$=0.126, and $[p]^{num}_{\Gamma_{14}}$= 0.135. These values show how well the pressure field fulfilled the Laplace law, (2.12). For more details about this numerical experiment, the reader is referred to [60].

6 Conclusions

In this paper, we reviewed the recent development of phase-field models and their numerical methods for multi-component fluid flows with interfacial phenomena. The models consist of a Navier-Stokes system coupled with a multi-component Cahn-Hilliard system through a phase-field dependent surface tension force, variable density and viscosity, and the advection term. The classical infinitely thin boundary of separation between two immiscible fluids is replaced by a transition region of a small but finite width, across which the composition of the mixture changes continuously. A constant level set of the phase-field is used to capture the interface between two immiscible fluids. The phase-field methods are capable of computing topological changes such as splitting and merging, and thus have been applied successfully to multi-component fluid flows involving large interface deformations. Practical applications such as non-Newtonian, microtube, and droplet impact flows were provided to illustrate the usefulness of using a phase-field method. Computational results showing the accuracy and effectiveness of phase-field models were given for various experiments.

Acknowledgments

This research was supported by Basic Science Research Program through the National Research Foundation of Korea (NRF) funded by the Ministry of Education, Science and

Technology (No. 331-2008-1-C00044). The author thanks his graduate students, Darae Jeong, Hyun Geun Lee, and Yibao Li for their help in preparing data and figures. The author also thanks his Ph.D. advisor, Professor John Lowengrub, for intellectual guidance during his Ph.D. and postdoctoral period. The author thanks the reviewers for the constructive and helpful comments on the revision of this article.

References

[1] R. Acar, Simulation of interface dynamics: a diffuse-interface model, Visual Comput., 25 (2009), 101–115.
[2] A. S. Almgren, J. B. Bell, P. Colella, L. H. Howell and M. L. Welcome, A conservative adaptive projection method for the variable density incompressible Navier-Stokes equations, J. Comput. Phys., 142 (1998), 1–46.
[3] W. F. Ames, Numerical Methods for Partial Differential Equations, Academic Press, San Diego, 1992.
[4] D. M. Anderson, G. B. McFadden and A. A. Wheeler, Diffuse-interface methods in fluid mechanics, Ann. Rev. Fluid Mech., 30 (1998), 139–165.
[5] V. E. Badalassi and S. Banerjee, Nano-structure computation with coupled momentum phase ordering kinetics models, Nucl. Eng. Des., 235(10-12) (2005), 1107–1115.
[6] V. E. Badalassi, H. D. Ceniceros and S. Banerjee, Computation of multiphase systems with phase field models, J. Comput. Phys., 190 (2003), 371–397.
[7] J. W. Barrett, J. F. Blowey and H. Garcke, Finite element approximation of the Cahn-Hilliard equation with degenerate mobility, SIAM J. Numer. Anal., 37 (1999), 286–318.
[8] J. W. Barrett, J. F. Blowey and H. Garcke, On fully practical finite element approximations of degenerate Cahn-Hilliard systems, M2AN Math. Model. Numer. Anal., 35 (2002), 713–748.
[9] J. Bell, P. Collela and H. Glaz, Second-order projection method for the incompressible Navier-Stokes equations, J. Comput. Phys., 85 (1989), 257–283.
[10] M. J. Berger and I. Rigoustsos, Technical Report NYU-501, New York University-CIMS, 1991.
[11] J. F. Blowey, M. I. M. Copetti and C. M. Elliott, Numerical analysis of a model for phase separation of a multi-component alloy, IMA J. Numer. Anal., 16 (1996), 111–139.
[12] R. Borcia and M. Bestehorn, Phase-field for Marangoni convection in liquid-gas systems with a deformable interface, Phys. Rev. E, 67 (2003), 066307.
[13] F. Boyer, A theoretical and numerical model for the study of incompressible mixture flows, Comput. Fluids, 31(1) (2002), 41–68.
[14] F. Boyer and C. Lapuerta, Study of a three component Cahn-Hilliard flow model, M2AN, 40(4) (2006), 653–687.
[15] F. Boyer, C. Lapuerta, S. Minjeaud, B. Piar and M. Quintard, Cahn-Hilliard/Navier-Stokes model for the simulation of three-phase flows, Transp. Porous Media, 2009.
[16] J. U. Brackbill, D. B. Kothe and C. Zemach, A continuum method for modeling surface tension, J. Comput. Phys., 100 (1992), 335–354.
[17] L. A. Caffarelli and N. E. Muler, An L^∞ bound for solutions of the Cahn-Hilliard equation, Arch. Rational Mech. Anal., 133 (1995), 129–144.
[18] J. W. Cahn, Free energy of a nonuniform system II: thermodynamic basis, J. Chem. Phys., 30 (1959), 1121–1124.
[19] J. W. Cahn, On spinodal decomposition, Acta Metall., 9 (1961), 795–801.

[20] J. W. Cahn and J. E. Hilliard, Free energy of a non-uniform system I: interfacial free energy, J. Chem. Phys., 28 (1958), 258–267.
[21] J. W. Cahn and J. E. Hilliard, Free energy of a nonuniform system III: nucleation in a two-component incompressible fluid, J. Chem. Phys., 31 (1959), 688–699.
[22] H. D. Ceniceros, R. L. Nos and A. M. Roma, Three-dimensional, fully adaptive simulations of phase-field fluid models, J. Comput. Phys., 229 (2010), 6135–6155.
[23] M. Chacha, S. Radeev, L. Tadrist and R. Occelli, Numerical treatment of the instability and breakup of a liquid capillary column in a bounded immiscible phase, Int. J. Multiphase Flow, 23 (1997), 377–395.
[24] Y. C. Chang, T. Y. Hou, B. Merriman and S. Osher, A level set formulation of Eulerian interface capturing methods for incompressible fluid flows, J. Comput. Phys., 124 (1996), 449–464.
[25] R. Chella and J. Viñals, Mixing of a two-phase fluid by cavity flow, Phys. Rev. E, 53 (1996), 3832–3840.
[26] L. Q. Chen and J. Shen, Applications of semi-implicit Fourier-spectral method to phase field equations, Comput. Phys. Commun., 108 (1998), 147–158.
[27] A. J. Chorin, A numerical method for solving incompressible viscous flow problems, J. Comput. Phys., 2 (1967), 12–26.
[28] M. Dehghan, Finite difference procedures for solving a problem arising in modeling and design of certain optoelectronic devices, Math. Comput. Simul., 71 (2006), 16–30.
[29] H. Ding and P. D. M. Spelt, Wetting condition in diffuse interface simulations of contact line motion, Phys. Rev. E, 75 (2007), 046708.
[30] H. Ding, P. D. M. Spelt and C. Shu, Diffuse interface model for incompressible two-phase flows with large density ratios, J. Comput. Phys., 226 (2007), 2078–2095.
[31] C. M. Elliott and D. A. French, Numerical studies of the Cahn-Hilliard equation for phase separation, IMA J. Appl. Math., 38 (1987), 97–128.
[32] D. J. Eyre, `www.math.utah.edu/~eyre/research/methods/stable.ps`.
[33] D. J. Eyre, Computational and Mathematical Models of Microstructural Evolution, The Material Research Society, Warrendale, 1998.
[34] M. Fernandino and C. A. Dorao, The least squares spectral element method for the Cahn-Hilliard equation, Appl. Math. Model., 35 (2011), 797–806.
[35] P. C. Fife, Models for phase separation and their mathematics, Euro. J. Diff. Eqns., 48 (2000), 1–26.
[36] D. Furihata, A stable and conservative finite difference scheme for the Cahn-Hilliard Equation, Numer. Math., 87 (2001), 675–699.
[37] D. Furihata, T. Onda and M. Mori, A finite difference scheme for the Cahn-Hilliard equation based on a Lyapunov functional, GAKUTO Int. Series Math. Sci. Appl., 2 (1993), 347–358.
[38] H. Garcke, B. Nestler and B. Stoth, On anisotropic order parameter models for multi-phase systems and their sharp interface limits, Phys. D, 115 (1998), 87–108.
[39] D. Gilbarg and N. S. Trudinger, Elliptic Partial Differential Equations of Second Order, Classics in Mathematics, Springer-Verlag, Berlin, 2001.
[40] J. Glimm, J. W. Grove, X. L. Li, K. M. Shyue, Q. Zhang and Y. Zeng, Three-dimensional front tracking, SIAM J. Sci. Comput., 19 (1998), 703–727.
[41] H. Gomeza and T. J. R. Hughes, Provably unconditionally stable, second-order time-accurate, mixed variational methods for phase-field models, J. Comput. Phys., 230 (2011), 5310–5327.
[42] D. Gueyffier, J. Li, A. Nadim, R. Scardovelli and S. Zaleski, Volume-of-fluid interface tracking with smoothed surface stress methods for three-dimensional flows, J. Comput. Phys.,

152 (1999), 423–456.
[43] M. E. Gurtin, D. Polignone and J. Viñals, Two-phase binary fluids and immiscible fluids described by an order parameter, Math. Models Meth. Appl. Sci., 6 (1996), 815–831.
[44] F. H. Harlow and J. E. Welch, The MAC method: a computing technique for solving viscous, incompressible, transient fluid flow problems involving free surface, Phys. Fluids, 8 (1965), 2182–2189.
[45] Q. He, R. Glowinski and X. P. Wang, A least-squares/finite element method for the numerical solution of the Navier-Stokes-Cahn-Hilliard system modeling the motion of the contact line, J. Comput. Phys., 230 (2011), 4991–5009.
[46] Q. He and N. Kasagi, Phase-field simulation of small capillary-number two-phase flow in a microtube, Fluid Dyn. Res., 40(7-8) (2008), 497–509.
[47] D. Jacqmin, Calculation of two-phase Navier-Stokes flows using phase-field modeling, J. Comput. Phys., 155 (1999), 96–127.
[48] D. Jacqmin, Contact-line dynamics of a diffuse fluid interface, J. Fluid Mech., 402 (2000), 57–88.
[49] H. C. Kan, W. Shyy, H. S. Udaykumar, P. Vigneron and R. Tran-Son-Tay, Effects of nucleus on leukocyte recovery, Ann. Biomed. Eng., 27 (1999), 648–655.
[50] H. C. Kan, H. S. Udaykumar, W. Shyy and R. Tran-Son-Tay, Hydrodynamics of a compound drop with application to leukocyte modeling, Phys. Fluids, 10 (1998), 760–774.
[51] G. E. Karniadakis, M. Israeli and S. A. Orszag, High-order splitting methods for the incompressible Navier-Stokes equations, J. Comput. Phys., 97 (1991), 414–443.
[52] B. J. Keestra, P. C. J. V. Puyvelde, P. D. Anderson and H. E. H. Meijer, Diffuse interface modeling of the morphology and rheology of immiscible polymer blends, Phys. Fluids, 15(9) (2003), 2567–2575.
[53] V. V. Khatavkar, P. D. Anderson, P. C. Duineveld and H. H. E. Meijer, Diffuse interface modeling of droplet impact on a pre-patterned solid surface, Macromol. Rapid. Commun., 26 (2005), 298–303.
[54] V. V. Khatavkar, P. D. Anderson, P. C. Duineveld and H. H. E. Meijer, Diffuse-interface modelling of droplet impact, J. Fluid Mech., 581 (2007), 97–127.
[55] V. V. Khatavkar, P. D. Anderson and H. H. E. Meijer, Capillary spreading of a droplet in the partially wetting regime using a diffuse-interface model, J. Fluid Mech., 572 (2007), 367–387.
[56] J. S. Kim, A continuous surface tension force formulation for diffuse-interface models, J. Comput. Phys., 204(2) (2005), 784–804.
[57] J. S. Kim, A diffuse-interface model for axisymmetric immiscible two-phase flow, Appl. Math. Comput., 160 (2005), 589–606.
[58] J. S. Kim, A numerical method for the Cahn-Hilliard equation with a variable mobility, Commun. Nonlinear Sci. Numer. Simul., 12 (2007), 1560–1571.
[59] J. S. Kim, Phase field computations for ternary fluid flows, Comput. Meth. Appl. Mech. Eng., 196 (2007), 4779–4788.
[60] J. S. Kim, A generalized continuous surface tension force formulation for phase-field models for immiscible multi-component fluid flows, Comput. Meth. Appl. Mech. Eng., 198 (2009), 3105–3112.
[61] J. S. Kim and H.-O. Bae, An unconditionally gradient stable adaptive mesh refinement for the Cahn-Hilliard equation, JKPS, 53(2) (2008), 672–679.
[62] J. S. Kim and K. Kang, A numerical method for the ternary Cahn-Hilliard system with a degenerate mobility, Appl. Numer. Math., 59 (2009), 1029–1042.
[63] J. S. Kim, K. K. Kang and J. S. Lowengrub, Conservative multigrid methods for Cahn-

Hilliard fluids, J. Comput. Phys., 193 (2004), 511–543.
[64] J. S. Kim and J. S. Lowengrub, Phase field modeling and simulation of three-phase flows, Int. Free Bound., 7 (2005), 435–466.
[65] C.-H. Kim, S.-H. Shin, H. G. Lee and J. S. Kim, A phase-field model for the pinchoff of liquid-liquid jets, JKPS, 55 (2009), 1451–1460.
[66] H. Kiwata, Instability of interfaces in phase-separating binary fluids at a finite Reynolds number, Phys. Fluids, 15 (2003), 2480–2485.
[67] H. G. Lee and J. S. Kim, Accurate contact angle boundary conditions for the Cahn-Hilliard equations, Comput. Fluids, 44 (2011), 178–186.
[68] H. G. Lee, K. M. Kim and J. S. Kim, On the long time simulation of the Rayleigh-Taylor instability, Int. J. Numer. Meth. Eng., 85 (2011), 1633–1647.
[69] H. Y. Lee, J. S. Lowengrub and J. Goodman, Modeling pinchoff and reconnection in a Hele-Shaw cell I: the models and their calibration, Phys. Fluids, 14(2) (2002), 492–513.
[70] H. Y. Lee, J. S. Lowengrub and J. Goodman, Modeling pinchoff and reconnection in a Hele-Shaw cell II: analysis and simulation in the nonlinear regime, Phys. Fluids, 14(2) (2002), 514–545.
[71] J. Li and Y. Renardy, Numerical study of flows of two immiscible liquids at low Reynolds number, SIAM Rev., 42(3) (2000), 417–439.
[72] J. Lighthill, Waves in Fluids, Cambridge University Press, Cambridge, 1978.
[73] C. Liu and J. Shen, A phase field model for the mixture of two incompressible fluids and its approximation by a Fourier-spectral method, Phys. D, 179 (2003), 211–228.
[74] J. S. Lowengrub and L. Truskinovsky, Quasi-incompressible Cahn-Hilliard fluids and topological transitions, Proc. R. Soc. Lond. A, 454 (1998), 2617–2654.
[75] D. F. Martin, P. Colella, M. Anghel and F. L. Alexander, Adaptive mesh refinement for multiscale nonequilibrium physics, Comput. Sci. Eng., 7 (2005), 24–31.
[76] I. N. Milosevic and E. K. Longmire, Pinch-off modes and satellite formation in liquid-liquid jet systems, Int. J. Multiphase Flow, 28(11) (2002), 1853–1869.
[77] A. Novick-Cohen and L. A. Segel, Nonlinear aspects of the Cahn-Hilliard equation, Phys. D, 10 (1984), 277–298.
[78] S. Osher and R. P. Fedkiw, Level set methods: an overview and some recent results, J. Comput. Phys., 169 (2001), 463–502.
[79] S. Osher and R. P. Fedkiw, Level Set Methods and Dynamic Implicit Surfaces, Springer-Verlag, New York, 2002.
[80] C. S. Peskin, The immersed boundary method, Acta Num., 11 (2002), 1–39.
[81] C. S. Peskin and D. M. McQueen, Modeling prosthetic heart valves for numerical analysis of blood flow in the heart, J. Comput. Phys., 37 (1980), 113–132.
[82] D. A. Porter and K. E. Easterling, Phase Transformations in Metals and Alloys, van Nostrand Reinhold, New York, 1993.
[83] W. H. Press, S. A. Teukolsky, W. T. Vetterling and B. P. Flannery, Numerical Recipes in C, Cambridge University Press, New York, 1993.
[84] J. S. Rowlinson and B. Widom, Molecular Theory of Capillarity, Dover Publications, New York, 2003.
[85] J. A. Sethian and P. Smereka, Level set methods for fluid interfaces, Annu. Rev. Fluid Mech., 35 (2003), 341–372.
[86] J. Shen and X. Yang, An efficient moving mesh spectral method for the phase-field model of two-phase flows, J. Comput. Phys., 228(8) (2009), 2978–2992.
[87] J. Shen and X. Yang, Energy stable schemes for Cahn-Hilliard phase-field model of two-

phase incompressible flows, Chin. Ann. Math., 31B(5) (2010), 743–758.
[88] K. A. Smith, F. J. Solis and D. L. Chopp, A projection method for motion of triple junctions by level sets, Int. Free Bound., 4 (2002), 263–276.
[89] V. N. Starovoitov, Model of the motion of a two-component liquid with allowance of capillary forces, J. Appl. Mech. Tech. Phys., 35 (1994), 891–897.
[90] Y. Sun and C. Beckermann, Diffuse interface modeling of two-phase flow based on averaging: mass and momentum equations, Phys. D, 198 (2004), 281–308.
[91] M. Sussman, A. S. Almgren, J. B. Bell, P. Colella, L. H. Howell and M. L. Welcome, An adaptive level set approach for incompressible two-phase flows, J. Comput. Phys., 148 (1999), 81–124.
[92] M. Sussman, P. Smereka and S. Osher, A level set approach for computing solutions to incompressible two-phase flow, J. Comput. Phys., 114 (1994), 146–159.
[93] K. E. Teigen, P. Song, J. Lowengrub and A. Voigt, A diffuse-interface method for two-phase flows with soluble surfactants, J. Comput. Phys., 230 (2011), 375–393.
[94] S. Tomotika, On the instability of a cylindrical thread of a viscous liquid surrounded by another viscous fluid, Proc. Roy. Soc. A, 150 (1935), 322–327.
[95] U. Trottenberg, C. Oosterlee and A. Schüller, MULTIGRID, Academic press, London, 2001.
[96] H. S. Udaykumar, H. C. Kan, W. Shyy and R. Tran-Son-Tay, Multiphase dynamics in arbitrary geometries on fixed Cartesian grids, J. Comput. Phys., 137 (1997), 137–366.
[97] E. Uzgoren, J. Sin and W. Shyy, Marker-based, 3-D adaptive cartesian grid method for multiphase flow around irregular geometries, Commun. Comput. Phys., 5(1) (2009), 1–41.
[98] M. Verschueren, F. N. Van De Vosse and H. E. H. Heijer, Diffuse-interface modelling of thermocapillary flow instabilities in a Hele-Shaw cell, J. Fluid Mech., 434 (2001), 153–166.
[99] W. Villanueva, J. Sjodahl, M. Stjernstrom, J. Roeraade and G. Amberg, Microdroplet deposition under a liquid medium, Lanmuir, 23 (2007), 1171–1177.
[100] B. P. Vollmayr-Lee and A. D. Rutenberg, Fast and accurate coarsening simulation with an unconditionally stable time step, Phys. Rev. E, 68 (2003), 066703.
[101] S. Wise, J. S. Kim and J. S. Lowengrub, Solving the regularized, strongly anisotropic Cahn-Hilliard equation by an adaptive nonlinear multigrid method, J. Comput. Phys., 226 (2007), 414–446.
[102] X. Yang, J. J. Feng, C. Liu and J. Shen, Numerical simulations of jet pinching-off and drop formation using an energetic variational phase-field method, J. Comput. Phys., 218 (2006), 417–428.
[103] T. Young, An essay on the cohesion of fluids, Trans. R. Soc. Lond., 95 (1805), 65–87.
[104] P. Yue and J. J. Feng, Wall energy relaxation in the Cahn-Hilliard model for moving contact lines, Phys. Fluids, 23 (2011), 012106.
[105] P. Yue, J. J. Feng, C. Liu and J. Shen, A diffuse-interface method for simulating two-phase flows of complex fluids, J. Fluid Mech., 515 (2004), 293–317.
[106] P. Yue, J. J. Feng, C. Liu and J. Shen, Diffuse-interface simulations of drop coalescence and retractio in viscoelastic fluids, J. Non-Newtonian Fluid Mech., 129 (2005), 163–176.
[107] P. Yue, C. Zhou and J. J. Feng, Spontaneous shrinkage of drops and mass conservation in phase-field simulations, J. Comput. Phys., 223 (2007), 1–9.
[108] S. Zhang and M. Wang, A nonconforming finite element method for the Cahn-Hilliard equation, J. Comput. Phys., 229 (2010), 7361–7372.
[109] J. Zhu, L. Q. Chen, J. Shen and V. Tikare, Coarsening kinetics from a variable-mobility Cahn-Hilliard equation: application of a semi-implicit Fourier spectral method, Phys. Rev. E, 60 (1999), 3564–3572.